

A Run-Group Proposal Submitted to PAC 45

Measurement of Deep Exclusive π^- Production using a Transversely Polarized ^3He Target and the SoLID Spectrometer

May 21, 2017

J. Arrington, K. Hafidi, M. Hattawy, P. Reimer, S. Riordan, Z. Ye*
Argonne National Laboratory, Physics Division, Argonne, IL, USA

Z. Ahmed*, G.R. Ambrose, S. Basnet, R.S. Evans, G.M. Huber[†], W. Li, D. Paudyal, Z. Papandreou
University of Regina, Regina, SK, Canada

H. Gao, X. Li, T. Liu, C. Peng, W. Xiong, X.F. Yan, Z. Zhao
Duke University, Durham, NC, USA

A. Camsonne, J-P. Chen, S. Covrig-Dusa, D. Gaskell
Jefferson Lab, Newport News, VA, USA

T. Breclj, M. Mihovilovič, S. Širca, S. Štajner
Jožef Stefan Institute and University of Ljubljana, Slovenia

K. Aniol
California State University – Los Angeles, Los Angeles, CA, USA

M. Boer
Los Alamos National Laboratory, Physics Division, Los Alamos, NM, USA

D. Dutta, L. Ye
Mississippi State University, Mississippi State, MS, USA

C. E. Hyde, F.R. Wesselmann
Old Dominion University, Norfolk, VA, USA

P. Markowitz
Florida International University, Miami, FL, USA

V. Sulkosky

University of Virginia, Charlottesville, VA, USA

E. Voutier

Institut de Physique Nucléaire IN2P3/CNRS, Université Paris Sud, Orsay, France

† Contact person , * Spokesperson

Abstract

We propose to measure the transverse nucleon, single-spin asymmetries $A_{UT}(\phi, \phi_S)$ in the exclusive $\bar{n}(e, e' \pi^-)p$ reaction, during the transversely polarized ^3He target SIDIS experiment (i.e. E12-10-006 [1]) with SoLID [2]. In principle, as many as six azimuthal modulations of the form $A_{UT}^{\sin(\mu\phi+\lambda\phi_S)}$ contribute (where μ and λ are integers) [3], but four of these modulations are small and the physics interest is concentrated in the largest two.

Our primary goal is the measurement of $A_{UT}^{\sin(\phi-\phi_S)}$. This polarization observable has been noted as being sensitive to the spin-flip generalized parton distribution (GPD) \tilde{E} , and factorization studies have indicated that precocious scaling is likely to set in at moderate $Q^2 \sim 2 - 4 \text{ GeV}^2$, as opposed to the absolute cross section, where scaling is not expected until $Q^2 > 10 \text{ GeV}^2$. Furthermore, this observable has been noted as being important for the reliable extraction of the charged pion form factor from pion electroproduction. Our secondary goal is the measurement of the $A_{UT}^{\sin(\phi_S)}$ asymmetry, which is sensitive to the higher twist transversity GPDs, and provides valuable information on transverse photon contributions at small $-t$. Both asymmetry datasets are projected to be of much higher quality than a pioneering measurement by HERMES [4]. The remaining four $A_{UT}^{\sin(\mu\phi+\lambda\phi_S)}$ modulations will also be measured, but are expected to be small.

This measurement is complementary to a proposal reviewed by PAC39 [5] for the SHMS+HMS in Hall C. The asymmetry that is most sensitive to \tilde{E} is the longitudinal photon, transverse nucleon, single-spin asymmetry $A_L^\perp(\sin(\phi - \phi_S))$ in exclusive charged pion electroproduction. The SHMS+HMS allow the L-T separation needed to reliably measure this quantity. However, the limited detector acceptance and the error-magnification inherent in an L-T separation necessitates the use of a next generation, externally polarized, continuous flow, high luminosity $^3\tilde{\text{He}}$ target based on a large volume polarizer and compressor being developed at the University of New Hampshire.

A wide $-t$ coverage is needed to obtain a good understanding of the asymmetries. Thus, it has always been intended to complement the SHMS+HMS $A_L^\perp(\sin(\phi - \phi_S))$ measurement with an unseparated $A_{UT}^{\sin(\phi-\phi_S)}$ measurement using a large solid angle detector. The high luminosity capabilities of SoLID make it well-suited for this measurement. Since an L-T separation is not possible with SoLID, the observed asymmetry is expected to be diluted by the ratio of the longitudinal cross section to the unseparated cross section. This was also true for the pioneering HERMES measurements, which provided a valuable constraint to models for the \tilde{E} GPD. In order to assure a clean measurement of exclusive π^- production, it is required to detect the recoil proton from the $\bar{n}(e, e' \pi^-)p$ reaction. We propose to analyze the E12-10-006 event files off-line to look for $e - \pi^- - p$ triple coincidence events in SoLID for the case where the proton is emitted $8^\circ < \theta < 24^\circ$. This has no impact upon E12-01-006 whatsoever, and yields valuable unseparated asymmetry data.

Contents

1	Scientific Justification	4
1.1	Generalized Parton Distributions and Contribution from the Pion Pole	4
1.2	Single spin asymmetry in exclusive pion electroproduction	6
1.3	The Complementarity of Separated and Unseparated Asymmetry Measurements	9
1.4	Motivation for and Status of the other Fourier Azimuthal Components	12
2	Experimental Method	16
2.1	Transversely Polarized ^3He Target	16
2.2	SoLID Spectrometer and Detectors	17
2.3	Recoil Proton Identification	18
2.4	Trigger Design	20
3	Projected Results	21
3.1	Kinematic Coverage	21
3.2	Estimated Rates	22
3.3	Asymmetry Projections	22
3.4	Missing Mass and Background	27
3.5	Systematic Uncertainties	29
4	Responses to Items Identified in the 2016 Review	30
4.1	SoLID Acceptance Simulations	30
4.2	Experimental Background	33
4.3	Resolution and Energy Loss	34
4.4	Projected Uncertainties	34
4.5	Fermi Momentum Effects	35
4.6	Dialog with Theorists	37
5	Summary	38
A	Monte Carlo model of Deep Exclusive π^- Production from the Neutron in ^3He	39
A.1	Definition of the Cross Section and Single-Spin Asymmetries	39
A.2	Cross Section Model for Higher Q^2 Kinematics	40
A.2.1	Constraints	40
A.2.2	Parametrization of σ_L , σ_T , σ_{LT} , & σ_{TT}	40
A.3	Parametrization of six Single-Spin Asymmetries	42
A.4	Target Neutron Fermi Momentum	43
A.5	Energy Loss and Multiple Scattering	43
A.6	Final State Interactions	44

1 Scientific Justification

1.1 Generalized Parton Distributions and Contribution from the Pion Pole

In recent years, much progress has been made in the theory of generalized parton distributions (GPDs). Unifying the concepts of parton distributions and of hadronic form factors, they contain a wealth of information about how quarks and gluons make up hadrons. The key difference between the usual parton distributions and their generalized counterparts can be seen by representing them in terms of the quark and gluon wavefunctions of the hadron. While the usual parton distributions are obtained from the squared hadron wavefunction representing the probability to find a parton with specified polarization and longitudinal momentum fraction x in the fast moving hadron (Fig. 1a), GPDs represent the interference of different wavefunctions, one where the parton has momentum fraction $x + \xi$ and one where this fraction is $x - \xi$ (Fig. 1b). GPDs thus correlate different parton configurations in the hadron at the quantum mechanical level. A special kinematic regime is probed in deep exclusive meson production, where the initial hadron emits a quark-antiquark or gluon pair (Fig. 1c). This has no counterpart in the usual parton distributions and carries information about $q\bar{q}$ and gg -components in the hadron wavefunction.

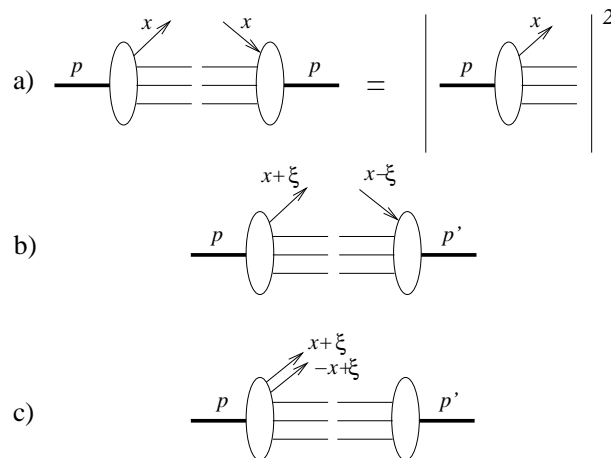


Figure 1: (a) Usual parton distribution, representing the probability to find a parton with momentum fraction x in the nucleon. (b) GPD in the region where it represents the emission of a parton with momentum fraction $x + \xi$ and its reabsorption with momentum fraction $x - \xi$. (c) GPD in the region where it represents the emission of a quark-antiquark pair, and has no counterpart in the usual parton distributions. This figure has been adapted from Ref. [6].

Apart from the momentum fraction variables x and ξ , GPDs depend on the four momentum transfer t . This is an independent variable, because the momenta p and p' may differ in either their longitudinal or transverse components. GPDs thus interrelate the longitudinal and transverse momentum structure of partons within a fast moving hadron.

In order to access the physics contained within GPDs, one is restricted to the hard scattering regime. An important feature of hard scattering reactions is the possibility to separate clearly the perturbative and non-perturbative stages of the interaction. Qualitatively speaking, the presence of a hard probe allows one to create small size quark-antiquark and gluon configurations, whose interactions are described by perturbative QCD (pQCD). The non-perturbative stage of the reaction describes how the hadron reacts to this configu-

ration, or how this probe is transformed into hadrons. This separation is the so-called factorization property of hard reactions. Deep Exclusive Meson electro-Production (DEMP) was first shown to be factorizable in Ref. [7]. This factorization applies when the virtual photon is longitudinally polarized, which is more probable to produce a small size configuration compared to a transversely polarized photon.

GPDs are universal quantities and reflect the structure of the nucleon independently of the reaction which probes the nucleon. At leading twist-2 level, the nucleon structure information can be parameterized in terms of four quark chirality conserving GPDs, denoted H , E , \tilde{H} and \tilde{E} . H and E are summed over quark helicity, while \tilde{H} and \tilde{E} involve the difference between left and right handed quarks. H and \tilde{H} conserve the helicity of the proton, while E and \tilde{E} allow for the possibility that the proton helicity is flipped. Because quark helicity is conserved in the hard scattering regime, the produced meson acts as a helicity filter. In particular, leading order QCD predicts that vector meson production is sensitive only to the unpolarized GPDs, H and E , whereas pseudoscalar meson production is sensitive only to the polarized GPDs, \tilde{H} and \tilde{E} . In contrast, deeply virtual Compton scattering (DVCS) depends at the same time on both the polarized (\tilde{H} and \tilde{E}) and the unpolarized (H and E) GPDs. This makes DEMF reactions complementary to the DVCS process, as it provides an additional tool to disentangle the different GPDs [8].

Besides coinciding with the parton distributions at vanishing momentum transfer ξ , the GPDs have interesting links with other nucleon structure quantities. Their first moments are related to the elastic form factors of the nucleon through model-independent sum rules [9]:

$$\sum_q e_q \int_{-1}^{+1} dx H^q(x, \xi, t) = F_1(t), \quad (1)$$

$$\sum_q e_q \int_{-1}^{+1} dx E^q(x, \xi, t) = F_2(t), \quad (2)$$

$$\sum_q e_q \int_{-1}^{+1} dx \tilde{H}^q(x, \xi, t) = G_A(t), \quad (3)$$

$$\sum_q e_q \int_{-1}^{+1} dx \tilde{E}^q(x, \xi, t) = G_P(t), \quad (4)$$

where e_q is the charge of the relevant quark, $F_1(t)$, $F_2(t)$ are the Dirac and Pauli elastic nucleon form factors, and $G_A(t)$, $G_P(t)$ are the isovector axial and pseudoscalar nucleon form factors. The t -dependence of $G_A(t)$ is poorly known, and although $G_P(t)$ is an important quantity, it remains highly uncertain because it is negligible at the momentum transfer of β -decay [10]. Because of partial conservation of the axial current (PCAC), $G_P(t)$ alone receives contributions from $J^{PG} = 0^{--}$ states [11], which are the quantum numbers of the pion, and so \tilde{E} contains an important pion pole contribution (Fig. 2).

Accordingly, Refs. [12, 13] have adopted the pion pole-dominated ansatz

$$\tilde{E}^{ud}(x, \xi, t) = F_\pi(t) \frac{\theta(\xi > |x|)}{2\xi} \phi_\pi\left(\frac{x + \xi}{2\xi}\right), \quad (5)$$

where $F_\pi(t)$ is the pion electromagnetic form factor, and ϕ_π is the pion distribution amplitude. In Ref. [14], to obtain a better description of the kinematic region accessible until the construction of the EIC, the perturbative (or one-gluon exchange) expression for F_π is replaced with a parameterization based on the experimental form factor, representing an additional soft contribution not (fully) related to \tilde{E} . Regardless of which expression is used, \tilde{E} cannot be related to already known parton distributions, and so experimental

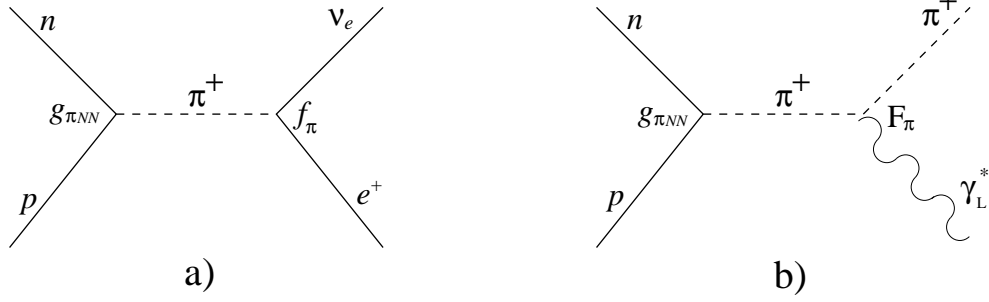


Figure 2: (a) Pion pole contribution to $G_P(t)$, and hence to \tilde{E} . (b) Pion pole contribution to meson electroproduction at low $-t$.

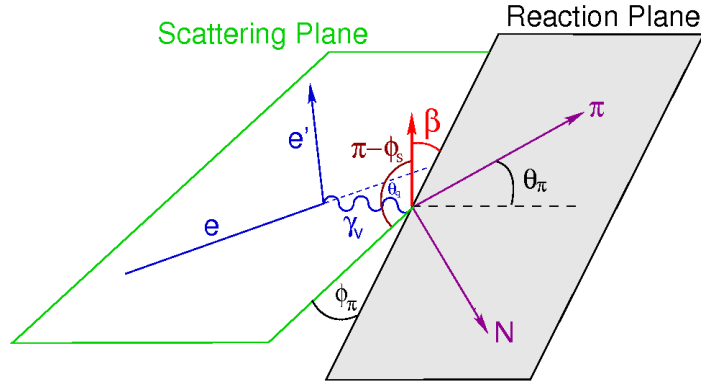


Figure 3: Scattering and hadronic reaction planes for exclusive $\vec{N}(e, e'\pi)N'$. ϕ is the azimuthal angle between the hadronic reaction plane and the electron scattering plane, and θ_q is the scattering angle of the virtual photon with respect to the incident electron beam. ϕ_s is the azimuthal angle between the target nucleon polarization and the scattering plane, and $\beta = (\phi - \phi_s)$ is the angle between the target nucleon polarization vector and the reaction plane.

information about \tilde{E} via DEMP can provide new information on nucleon structure which is unlikely to be available from any other source.

1.2 Single spin asymmetry in exclusive pion electroproduction

Frankfurt et al. [15] have considered a specific polarization observable which is the most sensitive observable to probe the spin-flip \tilde{E} . This variable is the single-spin asymmetry for exclusive charged pion production, $\vec{p}(e, e'\pi^+)n$ or $\vec{n}(e, e'\pi^-)p$, from a transversely polarized nucleon target, and is defined [13] as

$$A_L^\perp = \left(\int_0^\pi d\beta \frac{d\sigma_L^\pi}{d\beta} - \int_\pi^{2\pi} d\beta \frac{d\sigma_L^\pi}{d\beta} \right) \left(\int_0^{2\pi} d\beta \frac{d\sigma_L^\pi}{d\beta} \right)^{-1}, \quad (6)$$

where $d\sigma_L^\pi$ is the exclusive charged pion electroproduction cross section using longitudinally polarized photons and β is the angle between the nucleon polarization vector and the reaction plane (Fig. 3).

This asymmetry is related to the parton-helicity-conserving part of the scattering process and is sensitive

to the interference between \tilde{H} and \tilde{E} [3, 15]:

$$A_L^\perp = \frac{\sqrt{-t'}}{m_p} \frac{\xi \sqrt{1-\xi^2} \text{Im}(\tilde{E}^* \tilde{H})}{(1-\xi^2)\tilde{H}^2 - \frac{t\xi^2}{4m_p} \tilde{E}^2 - 2\xi^2 \text{Re}(\tilde{E}^* \tilde{H})}. \quad (7)$$

Frankfurt et al. [15] have shown that this asymmetry must vanish if \tilde{E} is zero. If \tilde{E} is not zero, the asymmetry will display a $\sin \beta$ dependence. Their predicted asymmetry using the \tilde{E} ansatz from Ref. [16] is shown in Fig. 4. This calculation is Q^2 -independent, depending only on how well the soft contributions cancel in the asymmetry.

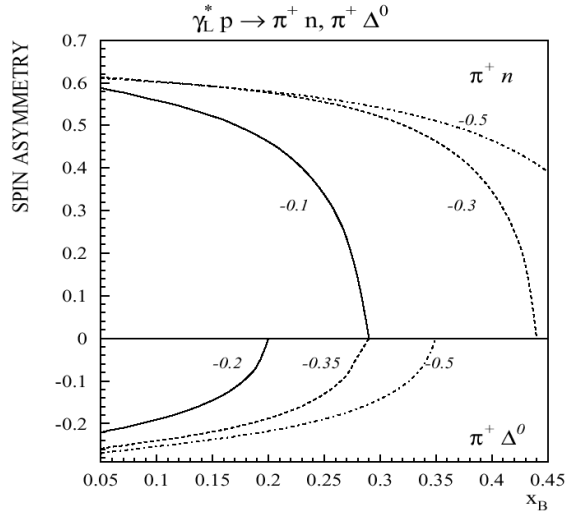


Figure 4: Transverse single-spin asymmetry for the longitudinal electroproduction of $\pi^+ n$ and $\pi^+ \Delta^0$ at different values of t [indicated on the curves in GeV^2]. The asymmetry drops to zero at the parallel kinematic limit, which is different for each t value, because the definition of β is ill-defined at this point. This figure is taken from Ref. [17].

It seems likely that a precocious factorization of the meson production amplitude into three parts – the overlap integral between the photon and pion wave functions, the hard interaction, and the GPD – will lead to a precocious scaling of A_L^\perp as a function of Q^2 at moderate $Q^2 \sim 2 - 4 \text{ GeV}^2$ [15]. This precocious scaling arises from the fact that higher twist corrections, which are expected to be significant at low Q^2 , will likely cancel when one examines the ratio of two longitudinal observables. In contrast, the onset of scaling for the absolute cross section is only expected for much larger values of $Q^2 > 10 \text{ GeV}^2$.

This point is made clear in Fig. 5. This figure shows renormalon model calculations [18] of both the asymmetry and the longitudinal cross section at $Q^2 = 4 \text{ GeV}^2$. While the magnitude of the cross section changes significantly when taking into account the twist-four corrections, A_L^\perp is essentially insensitive to them and displays the expected precocious scaling. The relatively low value of Q^2 for the expected onset of precocious scaling is important, because it should be experimentally accessible at Jefferson Lab. This places A_L^\perp among the most important GPD measurements that can be made in the meson scalar. If precocious scaling cannot be experimentally demonstrated in this ratio of two cross sections, then it may not be possible to determine GPDs from DEMP data.

Refs. [8] and [17] also point out that the study of the transverse target single-spin asymmetry versus t is important for the reliable extraction of the pion form factor from electroproduction experiments (Fig.

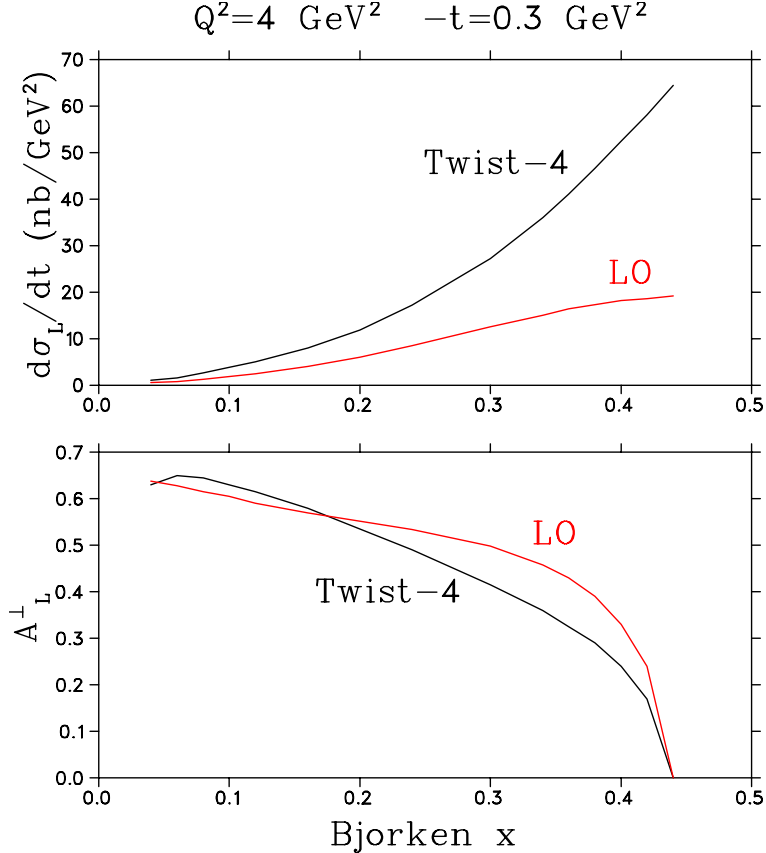


Figure 5: Calculation of the longitudinal photon transverse nucleon spin asymmetry including twist-four corrections by A. Belitsky [18] at $-t = 0.3 \text{ GeV}^2$, $Q^2=4 \text{ GeV}^2$. The red curves are the leading order calculation, while the black curves have twist-four power effects taken into account. While the cross section is very sensitive to these corrections, the transverse spin asymmetry is stable.

2b). Investigations of hard exclusive π^+ electroproduction using a pQCD factorization model [19,20] find that at $x_B = 0.3$ and $-t = -t_{min}$, the pion pole contributes about 80% of the longitudinal cross section. Since the longitudinal photon transverse single-spin asymmetry is an interference between pseudoscalar and pseudovector contributions, its measurement would help constrain the non-pole pseudovector contribution, and so assist the more reliable extraction of the pion form factor. The upper $Q^2 = 6 \text{ GeV}^2$ limit of the approved pion form factor measurements in the JLab 12 GeV program [21] is dictated primarily by the requirement $-t_{min} < 0.2 \text{ GeV}^2$, to keep non-pion pole contributions to σ_L at an acceptable level [19]. Transverse target single-spin asymmetry studies versus t may eventually allow, with theoretical input, the use of somewhat larger $-t$ data for pion form factor measurements, ultimately extending the Q^2 -reach of pion form factor data acquired with JLab 12 GeV beam. Thus, measurements of the transverse single-spin asymmetry are a logical step in the support of the pion form factor program.

1.3 The Complementarity of Separated and Unseparated Asymmetry Measurements

The reaction of interest is ${}^3\text{He}(e, e'\pi^-)p(pp)_{sp}$. The measurement of the transverse single-spin asymmetry requires the detection of the π^- in non-parallel kinematics. It is the component of the target polarization parallel to $\hat{q} \times \hat{p}_\pi$ that is important, and this direction is uniquely defined only in non-parallel kinematics.

Experimentally, the angle between the target polarization and the reaction plane, β , and the angle between the scattering and reaction planes, ϕ , are not independent. If the target polarization is at some angle, ϕ_s , relative to the scattering plane, then $\beta = \phi - \phi_s$.

The polarized nucleon cross section can be expressed [3, 22] in terms of these variables as:

$$d\sigma_{UT}(\phi, \phi_s) = \sum_k d\sigma_{UT_k}(\phi, \phi_s) = -\frac{P_\perp \cos \theta_q}{\sqrt{1 - \sin^2 \theta_q \sin^2 \phi_s}} \left[\begin{aligned} &\sin \beta \text{Im}(\sigma_{++}^{+-} + \epsilon \sigma_{00}^{+-}) \\ &+ \sin \phi_s \sqrt{\epsilon(1 + \epsilon)} \text{Im}(\sigma_{+0}^{+-}) \\ &+ \sin(\phi + \phi_s) \frac{\epsilon}{2} \text{Im}(\sigma_{++}^{+-}) \\ &+ \sin(2\phi - \phi_s) \sqrt{\epsilon(1 + \epsilon)} \text{Im}(\sigma_{+0}^{-+}) \\ &+ \sin(3\phi - \phi_s) \frac{\epsilon}{2} \text{Im}(\sigma_{+-}^{-+}) \end{aligned} \right], \quad (8)$$

where the $\cos \theta_q$ factor is needed to convert the target P_\perp relative to the lepton beam to that relative to the virtual photon (in accordance with the Trento convention), and much smaller factors proportional to $\sin \theta_q$ have been neglected for clarity. The σ_{mn}^{ij} correspond to nucleon polarizations $ij = (+\frac{1}{2}, -\frac{1}{2})$ and photon polarizations $mn = (+1, 0, -1)$, and $\sigma_T = \frac{1}{2}(\sigma_{++}^{++} + \sigma_{+-}^{--})$, $\sigma_L = \sigma_{00}^{++}$ are the usual unpolarized transverse and longitudinal cross sections.

From the above equation, it is clear that to extract A_L^\perp it is necessary to first isolate the $\sin \beta$ Fourier component of the polarized nucleon cross section. Once that has been accomplished, one must then separate the desired σ_{00}^{+-} term from the σ_{++}^{+-} term via a Rosenbluth-type separation. All of the other polarized terms can be distinguished from their respective azimuthal dependences, without need of a Rosenbluth separation [3].

It has not yet been possible to perform an experiment to measure A_L^\perp . The conflicting experimental requirements of transversely polarized target, high luminosity, L-T separation, and closely controlled systematic uncertainty, make this an exceptionally challenging observable to measure. The SHMS+HMS is the only facility with the necessary resolution and systematic error control to allow a measurement of A_L^\perp . However, the beamtime required to do a good measurement with current polarized target technology is in the range of 10^3 days. To minimize the beamtime required, PR12-12-005 [5] proposed the use of a next generation, externally polarized, continuous flow, high luminosity ${}^3\text{He}$ target based on a large volume polarizer and compressor developed at the University of New Hampshire. The science case for this measurement was favorably reviewed by PAC39, and they encouraged the continued development of the target technology. Although the New Hampshire group is making continued progress on the development of the target, there is no timeline for its actual implementation at Jefferson Lab.

The most closely related measurement, of the transverse single-spin asymmetry in exclusive π^+ electroproduction without an L-T separation, was published by the HERMES Collaboration in 2010 [4]. Their data were obtained for average values of $\langle x_B \rangle = 0.13$, $\langle Q^2 \rangle = 2.38 \text{ GeV}^2$ and $\langle t' \rangle = -0.46 \text{ GeV}^2$, subject

to the criterion $W^2 > 10 \text{ GeV}^2$. The six Fourier amplitudes in terms of the azimuthal angles ϕ , ϕ_s of the pion-momentum and proton-polarization vectors relative to the lepton scattering plane were determined. Of these, at leading twist only the $\sin \beta_{UT}$ Fourier amplitude receives a contribution from longitudinal photons. If one assumes that longitudinal contributions dominate, these $A_{UT}^{\sin(\phi-\phi_s)}$ values can be compared to GPD models for \tilde{E} , \tilde{H} .

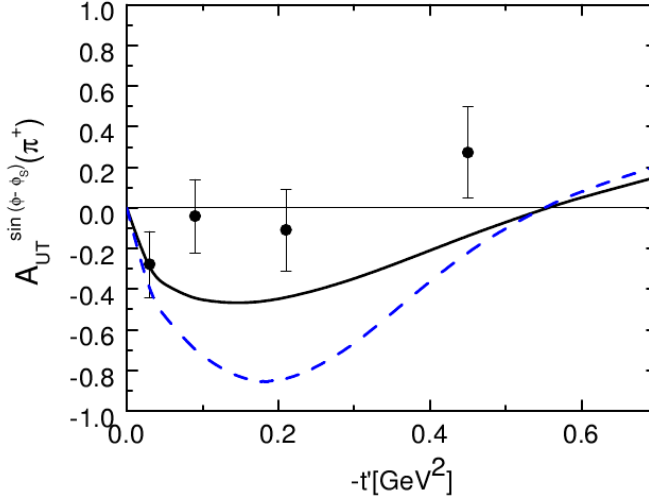


Figure 6: Predictions by Goloskokov and Kroll for the $\sin(\phi-\phi_s)$ moment of A_{UT} in the handbag approach, in comparison to the data from HERMES at $Q^2 = 2.45 \text{ GeV}^2$, $W = 3.99 \text{ GeV}$. Please note that the HERMES data follow the Trento convention, while the Eqns. 6, 7 and Figs. 4, 5 do not, leading to a normalization difference of $-\pi/2$ [22]. The independent variable is $-t' = |t - t_{min}|$. Dashed line: contribution from longitudinal photons only. Solid line: full calculation including both transverse and longitudinal photons. This figure is taken from Ref. [14].

Because transverse photon amplitudes are suppressed by $1/Q$, at very high Q^2 it is safe to assume that all observed meson production is due to longitudinal photons. At the lower Q^2 typical of the JLab and HERMES programs, however, this is not the case. Handbag-approach calculations by Goloskokov and Kroll [14] indicate much of the unseparated cross section measured by HERMES [4] is due to contributions from transversely polarized photons. In addition, there are contributions to $A_{UT}^{\sin(\phi-\phi_s)}$ from the interference between two amplitudes, both for longitudinal photons, as well as transverse photons [3]. At the amplitude level, the transverse suppression is given by μ/Q , where $\mu \sim 2 \text{ GeV}$ is a mass parameter given by the pion mass enhanced by the large ratio between the pion mass and the sum of the u and d current quark masses (chiral condensate). For experimentally accessible Q^2 , hardly any suppression of the twist-3 contribution is expected. As indicated in Fig. 6, the contribution from transverse photons tends to make the asymmetry smaller. At the HERMES kinematics, the dilution caused by transverse photons is about 50%. Although the observed unseparated asymmetry is small, the HERMES data are consistent with GPD models based on the dominance of \tilde{E} over \tilde{H} at low $-t'$. Indeed, the change in sign in the model curves at large $-t'$ in Fig. 6 is due to the large contribution from \tilde{E} demanded by the data [14]. An improved measurement of the transverse target spin asymmetry, in particular the $\sin(\phi - \phi_s)$ modulation, is clearly a high priority.

A run-group proposal concurrent with the SoLID transversely polarized ^3He SIDIS experiment allows for an unseparated asymmetry measurement to be obtained on a sooner timescale than the Hall C measurement.

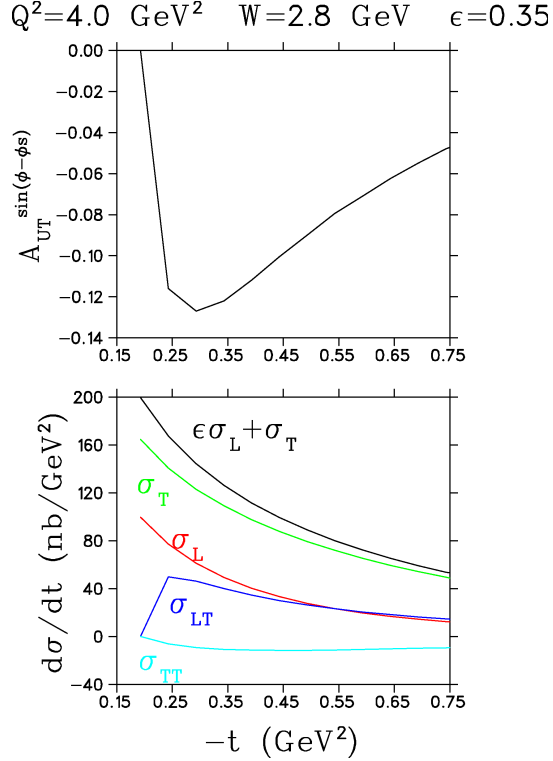


Figure 7: Calculation of the cross section components and $\sin(\phi - \phi_s)$ moment of the transverse nucleon spin asymmetry A_{UT} in the handbag approach by Goloskokov and Kroll [24] for kinematics similar to those in Fig. 5. Our measurement will be at higher $0.55 < \epsilon < 0.75$ than the $\epsilon = 0.35$ kinematics of this figure, so the dilution in the asymmetry will be significantly less.

In comparison to the HERMES measurement, the experiment proposed here will probe higher Q^2 and x_B , with much smaller statistical errors over a wider range of $-t$. SoLID will allow the first measurement for $Q^2 > 4 \text{ GeV}^2$, where GPD-based calculations are expected to apply. Thus, the measurements should be more readily interpretable than those from HERMES. Similar measurements using CLAS-12 and a transversely polarized ^1H target have been discussed previously [23], but this measurement will allow for smaller statistical uncertainties, due to SoLID's higher luminosity capabilities.

Handbag model calculations by Goloskokov and Kroll [24] shed further light on the expected asymmetry dilution. The bottom panel of Fig. 7 shows their predictions for the cross section components in exclusive charged pion production. Although their calculations tend to underestimate the σ_L values measured in the JLab $F_\pi - 2$ experiment [25], their model is in reasonable agreement with the unseparated cross sections [14]. They predict significant transverse contributions for JLab kinematics. A comparison of the unseparated asymmetry at $-t = 0.3 \text{ GeV}^2$, $x_B = 0.365$ in Fig. 7 with the separated longitudinal asymmetry at the same values of x_B , $-t$ in Fig. 5 indicates a substantial dilution of the unseparated asymmetry due to transverse photon contributions, similar to that observed in Fig. 6.

In addition to allowing a measurement at $Q^2 > 4 \text{ GeV}^2$, a measurement by SoLID of $A_{UT}^{\sin(\phi - \phi_s)}$ will cover a fairly large range of $-t$, allowing the asymmetry to be mapped over its full range with good statistical uncertainties – from its required zero-value in parallel kinematics, through its maximum, and then back to near-zero or even positive at larger $-t$. The shape of the asymmetry curve versus $-t$, as well as its maximum

value, are critical information for comparison to GPD-based models.

1.4 Motivation for and Status of the other Fourier Azimuthal Components

An important point is that any model that describes exclusive pion production will need to describe not only the leading-twist Fourier amplitude $A_{UT}^{\sin(\phi-\phi_s)}$, but also the other contributions to the target-spin azimuthal asymmetry listed in Eqn. 8, providing additional GPD model constraints. Like HERMES, we plan to determine the full set of asymmetries from their azimuthal modulations,

$$A(\phi, \phi_s) = \frac{d\sigma_{UT}(\phi, \phi_s)}{d\sigma_{UU}(\phi)} = - \sum_k A_{UT}^{\sin(\mu\phi + \lambda\phi_s)_k} \sin(\mu\phi + \lambda\phi_s)_k, \quad (9)$$

where $d\sigma_{UU}$ is the unpolarized nucleon cross section in terms of the well-known L, T, LT and TT response functions. These asymmetries include all five terms listed in Eqn. 8, plus a small $\sin(2\phi + \phi_s)$ term proportional to $\sin\theta_q$ not listed there.

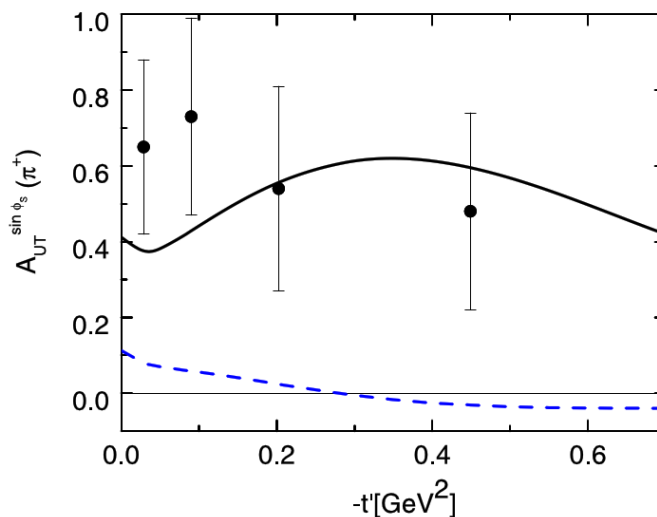


Figure 8: Data from HERMES for the $\sin(\phi_s)$ moment with a transversely polarized target at $Q^2 = 2.45 \text{ GeV}^2$, $W = 3.99 \text{ GeV}$. The solid line is the prediction of the handbag calculation by Goloskokov and Kroll under the assumption that the dominant transversity GPD is H_T and that the other three can be neglected. The dashed line is obtained disregarding the twist-3 contribution. This figure is taken from Ref. [14].

While most of the theoretical interest and the primary motivation of our experiment is the target asymmetry proportional to $\sin\beta$, there is growing interest in the $\sin(\phi_s)_{UT}$ asymmetry, as it may be interpretable in terms of the transversity GPDs. Independent of a specific dynamical interpretation (e.g. the handbag approach), the $A_{UT}^{\sin(\phi_s)}$ asymmetry will say something on the strength of the contributions from transverse photons at small $-t$ [14, 24],

$$A_{UT}^{\sin(\phi_s)} \sim \text{Im}[\mathcal{M}_{0+,++}^* \mathcal{M}_{0-,0+} - \mathcal{M}_{0-,++}^* \mathcal{M}_{0+,0+}], \quad (10)$$

where the helicities are in the order: pion neutron, photon proton, and the contribution of the transversity GPD H_T , in combination with a twist-3 meson wave function, enters as [26]:

$$\mathcal{M}_{0-,++} = e_0 \sqrt{1 - \xi^2} \int dx \mathcal{H}_{0-,++}^{\text{twist-3}} H_T. \quad (11)$$

In contrast to the $\sin(\phi - \phi_S)$ modulation, which has contributions from LL and TT interferences, the $\sin(\phi_s)$ modulation measures only the LT interference. The first term is proportional to t' , as is forced by angular momentum conservation, while the second one is not forced to vanish [24]. Indeed, HERMES measured the $\sin(\phi_s)$ modulation to be large and apparently nonzero at $-t' = 0$ (Fig. 8). Hence, both the amplitudes $\mathcal{M}_{0-,++}$ and $\mathcal{M}_{0+,0+}$ must be large, giving the first clear signal for strong contributions from transversely polarized photons at rather large values of W and Q^2 [14]. This is very interesting in its own right.

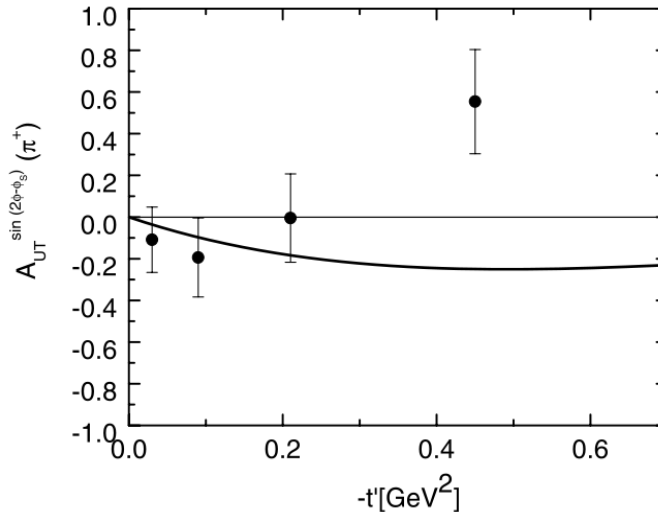


Figure 9: Data from HERMES for the $\sin(2\phi - \phi_s)$ moment with a transversely polarized target at $Q^2 = 2.45 \text{ GeV}^2$, $W = 3.99 \text{ GeV}$. The solid line is the prediction of the handbag calculation by Goloskokov and Kroll [14].

The calculation by Goloskokov and Kroll [14] for the $\sin(2\phi - \phi_S)$ modulation measured by HERMES is shown in Fig. 9. Both the experimental values, as well as the calculation, are small. The agreement is fairly good, except that the change of sign at large $-t'$ is not reproduced by the model. However, this observable is given by an interference between longitudinal amplitudes and transversal other than $\mathcal{M}_{0-,++}$, so an improvement of this moment probably requires a detailed modeling of the small transverse amplitudes contributing. The other three moments, $\sin(\phi + \phi_S)$, $\sin(2\phi + \phi_S)$ and $\sin(3\phi - \phi_S)$, are only fed by transverse-transverse interference terms and are therefore small in the handbag approach of Ref. [14].

A calculation for the kinematics of this experiment by S.V. Goloskokov and P. Kroll [14, 24, 26] for the amplitudes of the five azimuthal modulations listed in Eqn. 8 is shown in Fig. 10. It clearly shows that the two asymmetries of greatest physics interest dominate, while the other asymmetries are much smaller. This is consistent with the HERMES result, which found the four asymmetries $\sin(2\phi - \phi_s)$, $\sin(\phi + \phi_s)$, $\sin(3\phi - \phi_s)$, $\sin(2\phi + \phi_s)$, to be small over most of the measured t range (Fig. 11). This is good news, as large expected values for these asymmetries would complicate the extraction of the most-valued Fourier components.

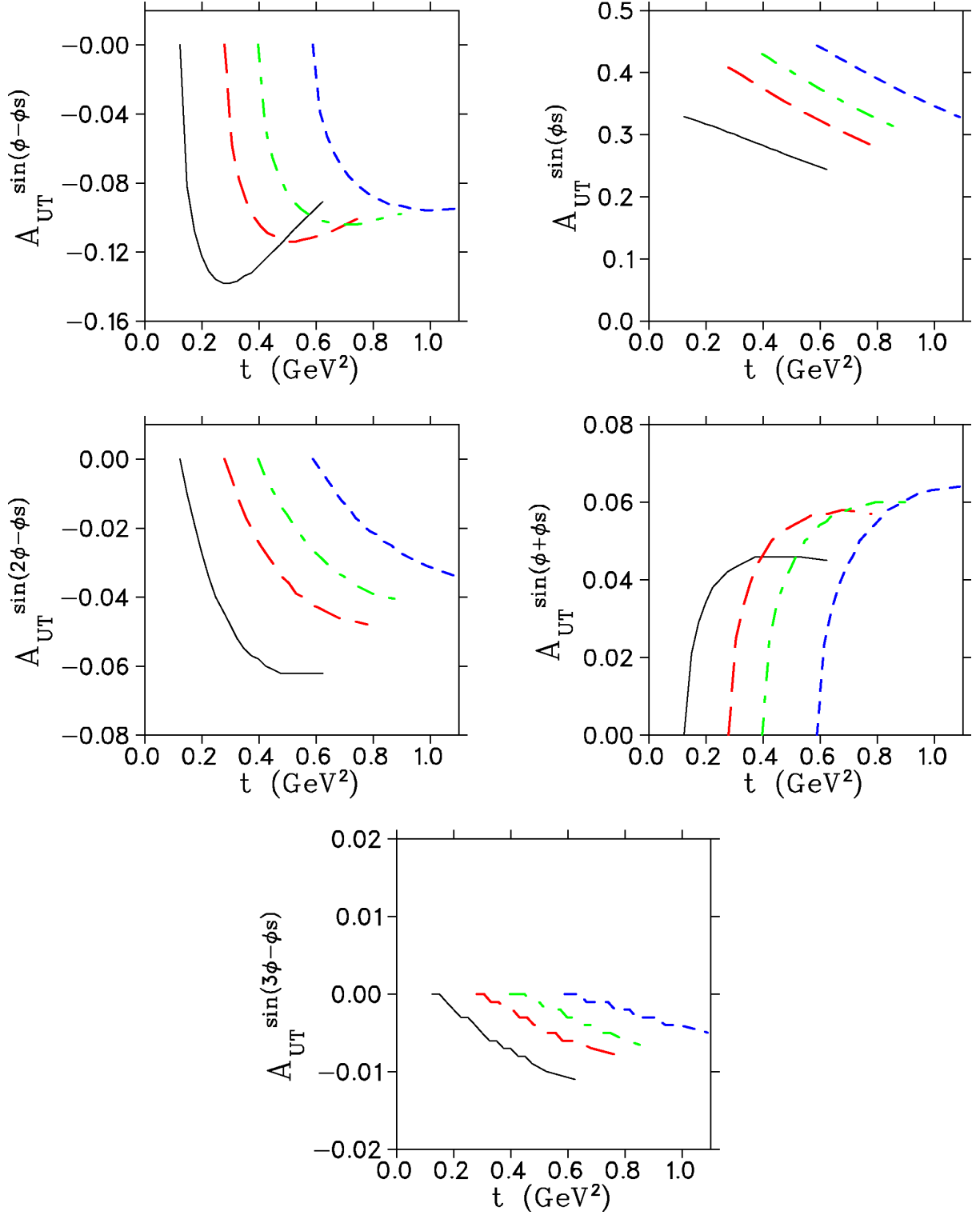


Figure 10: $\sin(\mu\phi + \lambda\phi_s)_k$ moments of the transverse nucleon spin asymmetry A_{UT} calculated in the handbag approach by Goloskokov and Kroll [24] for the kinematics of this experiment. Solid black: $Q^2 = 4.107$ GeV², $W = 3.166$ GeV; Long-dash red: $Q^2 = 5.138$ GeV², $W = 2.796$ GeV; Dash-dot green: $Q^2 = 6.049$ GeV², $W = 2.718$ GeV; Short-dash blue: $Q^2 = 6.894$ GeV², $W = 2.562$ GeV.

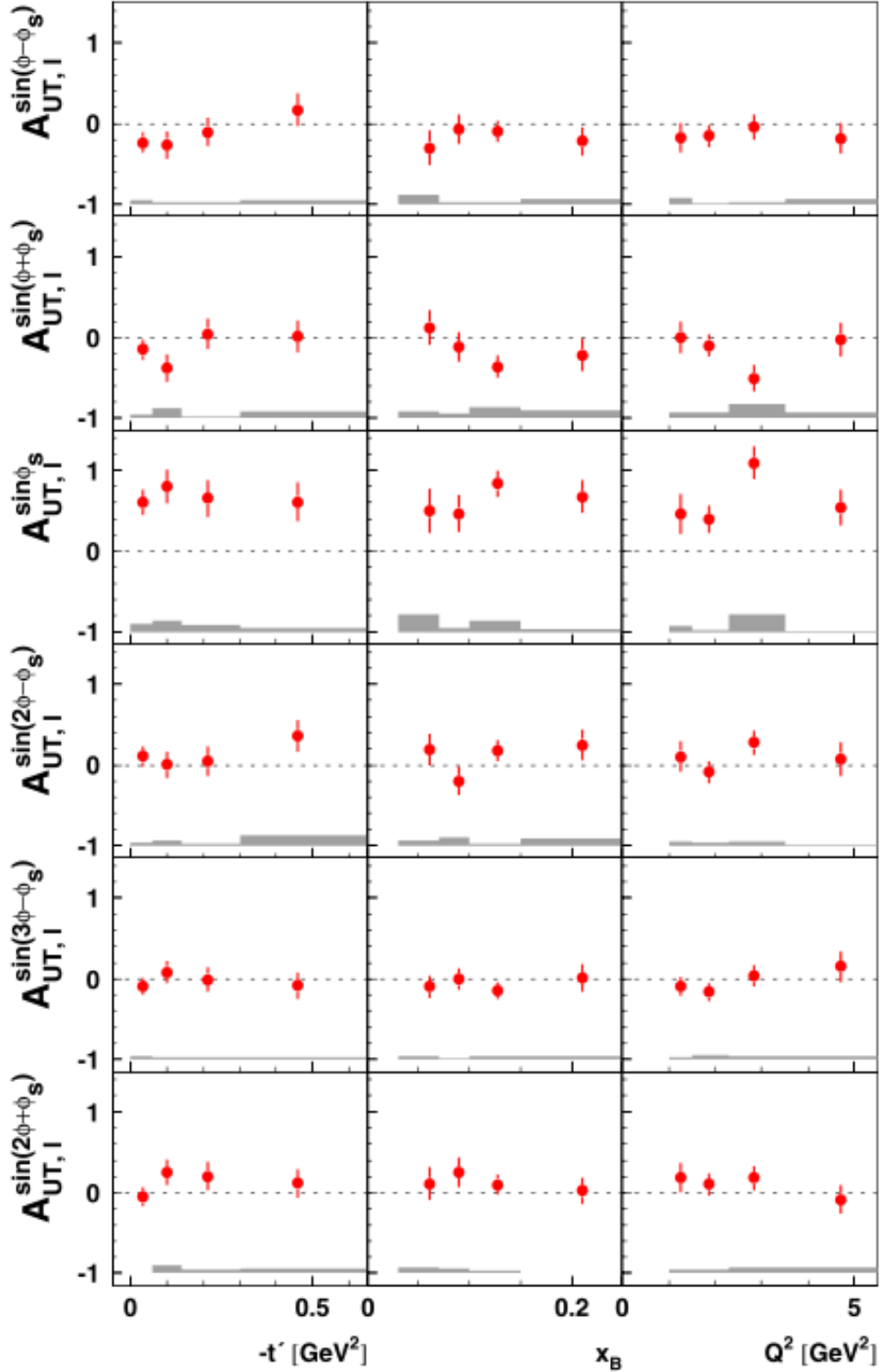


Figure 11: HERMES data for the set of six Fourier amplitudes $A_{UT}^{\sin(\phi-\phi_S)}$ describing the sine modulations of the single-spin azimuthal asymmetry. The error bars (bands) represent the statistical (systematic) uncertainties. The results receive an additional 8.2% scale uncertainty corresponding to the target polarization uncertainty. This figure is taken from Ref. [4].

2 Experimental Method

We propose to carry out the ${}^3\text{He}(e, e'\pi^-)p(pp)_{sp}$ measurement using the Solenoidal Large Intensity Device (SoLID [2]), in parallel with the already approved experiment, E12-10-006 [1], which will measure Semi-Inclusive Deep-Inelastic Scattering (SIDIS). Our discussion will concentrate on the region of clearest physics interpretation ($Q^2 > 4 \text{ GeV}^2$), even though lower Q^2 events will also be contained in the experimental data-set.

There are two SoLID configurations, called SoLID-SIDIS and SoLID-PVDIS. Besides E12-10-006, two SIDIS experiments, E12-11-007 [27] and E12-11-108 [28], along with the J/ψ experiment (E12-12-006 [29]), will also use the SoLID-SIDIS configuration. All of these experiments have been approved with A or A-rating. In addition, two “bonus-run” experiments, E12-10-006A [30] and E12-11-108A [31], have also been approved to run in parallel with the SIDIS experiments. The SoLID-PVDIS configuration is for the Parity Violation in Deep Inelastic Scattering (PVDIS) [32].

In order to assure a clean measurement of exclusive π^- production, it is required to tag the recoil proton from the $\bar{n}(e, e'\pi^-)p$ reaction. The existing SoLID detectors already have the capabilities of detecting protons from 8° up to 24° , while the main proton events from the DEMP process can cover 0° up to 50° . The experiment will use exactly the same setup and online production trigger as E12-10-006, which is the coincidence of electron triggers and hadron triggers from SoLID. We will perform the offline analysis to identify the recoil protons from DEMP and form the triple coincidence events together with electrons and π^- provided by SIDIS triggers. The discussion of proton detection is given in Sec. 2.3.

2.1 Transversely Polarized ${}^3\text{He}$ Target

Target	${}^3\text{He}$
Length	40 cm
Target Polarization	$\sim 60\%$
Target Spin Flip	≤ 20 mins
Target Dilution	90%
Effective Neutron	86.5%
Target Polarimetry Accuracy	$\sim 3\%$

Table 1: Key Parameters of the ${}^3\text{He}$ target.

The proposed measurement will utilize the same polarized ${}^3\text{He}$ target as E12-10-006 [1]. Such a target was successfully employed in E06-110, a 6 GeV SIDIS experiment in Hall A. A wide range of experiments have utilized polarized ${}^3\text{He}$ as an effective neutron target over a wide range of kinematics. And over the past decades several authors have calculated the effective neutron polarization in ${}^3\text{He}$ using three-nucleon wave functions and various models of the $N - N$ interaction [33]. These are now well established, and the error introduced by the uncertainty in the wave function is small.

Other nuclear effects which can influence the experimental asymmetry for a neutron bound inside ${}^3\text{He}$ include Fermi motion, off-shell effects, meson exchange currents, delta isobar contributions and π^- final state interactions. The exclusive nature of the process, the selected kinematics such as high Q^2 , large recoil

momentum and a complete coverage of the azimuthal angle ϕ ensures that corrections due to these nuclear effects will be small and can be modeled effectively.

The ^3He polarization direction is held by three sets of Helmholtz coils with a 25 Gauss magnetic field. Both the transverse and longitudinal directions can be provided by rotating the magnetic field. The ^3He gas, with density of about 10 atm (at 0°C), is stored in a 40 cm target cell made of thin glasses. With a $15\ \mu\text{A}$ electron beam, the neutron luminosity can be as high as $10^{36}\ \text{cm}^{-2}\text{s}^{-1}$. In-beam polarization of 60% was archived during the E06-110 experiment. Two kinds of polarimetry, NMR and EPR, were used to measure the polarization with relative 5% precision. We have plans to improve the accuracy of the measurement to reach 3%.

The target spin will be reversed for every 20 minutes by using the RF AFP technique. The additional polarization loss due to the spin reversal was kept at $< 10\%$, which has been taken into account in the overall 60% in-beam polarization. A new method for spin reversal using field rotation has been tested and was able to eliminate the polarization loss. Such an improvement will enable us to perform the spin-reversal in few minutes to reduce the target-spin-correlated systematic errors. The key parameters of the ^3He target are summarized in Table 1.

A collimator, similar to the one used in the E06-110, will be placed next to the target cell window to minimize the target cell contamination and to reduce the event rate. Several calibration targets will also be installed in this target system, including a multi-foil ^{12}C for optics study, a BeO target for beam tuning, and a reference target cell for dilution study and other calibration purposes.

2.2 SoLID Spectrometer and Detectors

The solenoid magnet for SoLID is based on the CLEO-II magnet built by Cornell University. The magnet is 3 m long with an inner cryostat diameter of 2.8 m. The field strength is greater than 1.35 Tesla, with an integrated BDL of 5 Tesla-meters. The fringe field at the front end after shielding is less than 5 Gauss. In the SIDIS-configuration, the CLEO-II magnet provides 2π acceptance in the azimuthal angle (ϕ) and covers polar angle (θ) from 8° up to 24° . The momentum acceptance is between 0.8 and 7.5 GeV/c for electrons and for hadrons, the momentum can be lower depending on the trigger efficiency. The momentum resolution is about 2%.

The layout of the SoLID detectors in the SIDIS-configuration is shown in Fig. 12. The detector system is divided into two regions for the forward-angle (FA) detection and the large-angle (LA) detection. Six tracking chambers based on Gas Electron Multipliers (GEM) will be used for charged particle tracking in the forward-angle region, and the first four of them will be shared by the large-angle region. In each region, a Shashlyk-type sampling EM calorimeter (LAEC or FAEC) will measure the particle energy and identify electrons from hadrons. A scintillator-pad detector (LASPD or FASPD) will be installed in front of each EC to reject photons and provide timing information. The forward-angle detectors will detect both the electrons and hadrons (mainly π^\pm). A light-gas Čerenkov detector (LGC) and a heavy-gas Čerenkov detector (HGC) will perform the e/π^\pm and π^\pm/K^\pm separation, respectively. The Multi-gas Resistive Plate Chamber (MRPC) will provide a precise timing measurement and serve as a backup of the FASPD on photon rejection. A more detailed discussion of the design, simulation, prototype-test of each detector is given in the SoLID preliminary conceptual design report (pCDR) [2].

Table 2 summarizes the key parameters of the detector system in the SIDIS configuration for both the

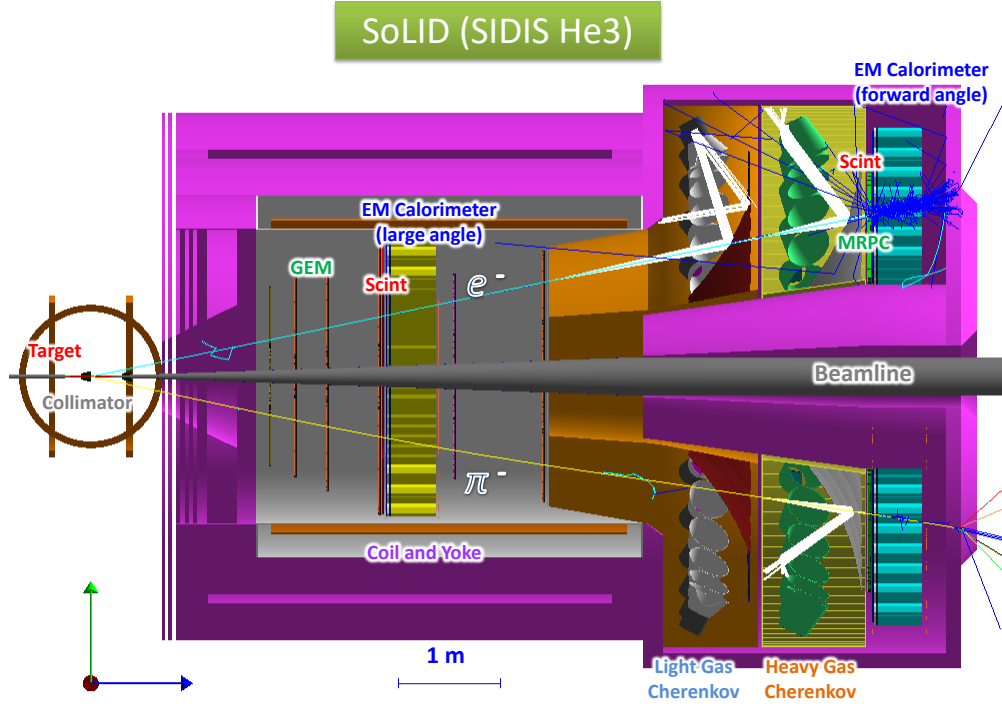


Figure 12: The Detector Layout of the SoLID-SIDIS configuration. The detector system includes six Gas Electron Multiplier (GEM) planes for charged particle tracking, two Scintillator Pad Detectors (SPD) followed by two Shashlyk sampling EM Calorimeters (EC) for energy measurement and particle identification, a Light Gas Čerenkov Detector (LGC) for $e-\pi^\pm$ separation, a Heavy Gas Čerenkov Detector (HGC) for $\pi^\pm-K^\pm$ separation, as well as a Multi-gap Resistive Plate Chamber (MRPC) for timing measurement. The first four GEM trackers, the first SPD (i.e. LASPD) and EC (i.e. LAEC) form the large-angle detection system for electron measurement. The forward-angle detection system, to measure electron and hadrons, is composed of all six GEM trackers, LGC, HGC, MRPC, the second SPD (i.e. FASPD) and the second EC (FAEC). The transversely polarized ^3He target field coils are shown to scale.

SIDIS and DEMP measurements.

2.3 Recoil Proton Identification

The cleanest way to identify the DEMP events is to detect all particles in the final state. The SoLID-SIDIS detector system has the capability of measuring electrons and pions, while protons can be isolated from other charged particles by using the time-of-flight (TOF) information. The TOF is provided by the timing detectors, including the MRPC and FASPD at the forward-angle detection region, and the LASPD at the large-angle detection region.

We examined the requirement of the timing resolution on these detectors by looking at the time difference between electrons and other heavier charged particles when they reach these detectors with the same momentum and flight path. As shown in the next section, the good protons from the DEMP reaction carry momenta from 0.3 GeV/c up to about 1.5 GeV/c, with angles from 0° to 50° . The FA-MRPC covers angles from 8° to 14.8° , and the angular range of the LASPD is from 16° to 24° . Hence we simulated events of electrons, pions, kaons and protons with the momentum from 0.3 GeV/c up to 1.5 GeV/c, and calculated

Experiments	SIDIS	DEMP
Reaction channel	$\vec{n}(e, e' \pi^\pm) X$	$\vec{n}(e, e' \pi^- p)$
Target	${}^3\text{He}$	same
Unpolarized luminosity	$\sim 10^{37} \text{ cm}^{-2}\text{s}^{-1}$ per nucleon	same
Momentum coverage	$>0.8 \text{ (GeV/c)}$ for e^-, π^\pm	same $0.3\text{-}1.5 \text{ (GeV/c)}$ for protons
Momentum resolution	$\sim 2\%$	same
Azimuthal angle coverage	$0^\circ\text{-}360^\circ$	same
Azimuthal angle resolution	5 mr	same
Polar angle coverage	$8^\circ\text{-}24^\circ$ for e $8^\circ\text{-}14.8^\circ$ for π^\pm	same same $8^\circ\text{-}24^\circ$ for p in SoLID
Polar angle resolution	0.6 mr	same
Target Vertex resolution	0.5 cm	same
Energy resolution on ECs	5%~10%	same
Trigger type	Double Coincidence $e^- + \pi^\pm$	same (online) Triple Coincidence $e^- + \pi^- + p$ (offline)
Expected DAQ rates	$<100 \text{ kHz}$	same (online)
Main Backgrounds	${}^3\text{He}(e, e' \text{K}^\pm / \pi^0) X$ Accidental Coincidence	${}^3\text{He}(e, e' \pi^\pm / \text{K}^\pm) X$ Accidental Coincidence
Key requirements	Radiation hardness Kaon Rejection DAQ	Proton Detection Exclusivity Timing Resolution

Table 2: Summary of Key Parameters for DEMP Measurement compared with SIDIS Experiments.

the time when they reach two different detectors with linear trajectories and at fixed angles.

The results are shown in Fig. 13. To clearly identify two types of charged particles with the same momentum, we normally require the timing difference between two particles to be larger than 5 times of the overall timing resolution, while the SoLID timing detectors can reach the resolution in the range of 150 ps down to 50 ps. At the FA-MRPC, which is more than 7 meters from the target, protons come 3 ns later than kaons, even at the highest momenta in the DEMP reaction. Hence, protons will be easily distinguished from other lighter particles. At the LA-SPD, which is about 3 meters away from the target, the time difference between protons and kaons is still more than 1 ns, which doesn't demand precise timing resolution.

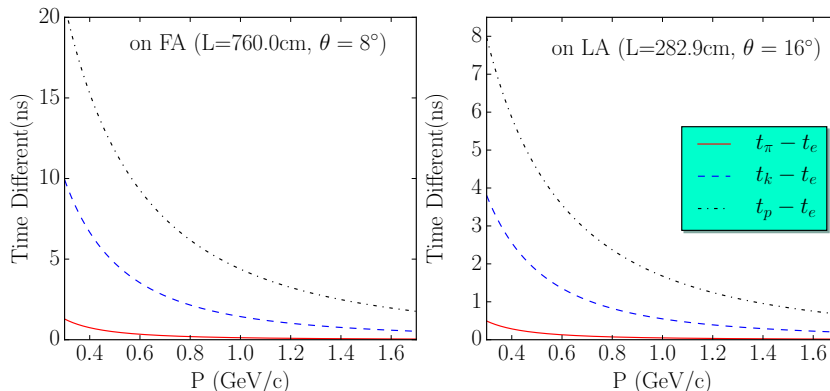


Figure 13: The time differences (in *ns*) between electrons and other charged particles, i.e. pions (red solid line), kaons (blue dashed line) and proton (black dash-dotted line), and their distributions as functions of particles' momentum at two different timing detectors, including the forward-angle (FA) MRPC and the large-angle (LA) SPD.

In general, the misidentified proton events can be mostly removed by cutting on the reconstructed missing quantities, e.g. angles, momenta and masses. The residual background will also be largely suppressed in the target-spin asymmetry extraction.

2.4 Trigger Design

In E12-10-006, the online production trigger will be the double-coincidence of the scattered electrons and hadrons. One will use the particle identification detectors, such as LGC, HGC and ECs, during the offline analysis to select π^\pm out from other hadrons. The DEMP events will be identified with the triple-coincidence of the scattered electron, π^- and proton, while the proton identification has been discussed above. We will use the same online trigger as the SIDIS one, and hence the new experiment will share exactly the same data-set as E12-10-006. The actual design of the SIDIS triggers will be far more complicated, and the detailed discussion of the trigger and DAQ designs is given in the SoLID pCDR [2].

3 Projected Results

To perform the simulation study and obtain the projected results, we developed a DEMP generator, as discussed in Appendix-A, and used it to generate events within a kinematic phase space slightly larger than the SoLID-SIDIS acceptance. The Fermi motion of the neutron in ^3He , radiation of the incident and scattered electrons, multiple scattering of the final state particles, and energy loss due to the ionization have been taken in account in this generator. Then, for every detected particle in each event, we added the acceptance profiles obtained from the GEANT4 simulation with the SoLID-SIDIS configuration and smeared the momenta and angles of the final state particles by the detector resolutions based on current knowledge from the tracking reconstruction study. We also compared the obtained distributions with GEMC simulations taking into account the target and individual detector geometries. To better simulate the real experimental conditions, we generated two sets of data with the target polarization up and down, respectively.

3.1 Kinematic Coverage

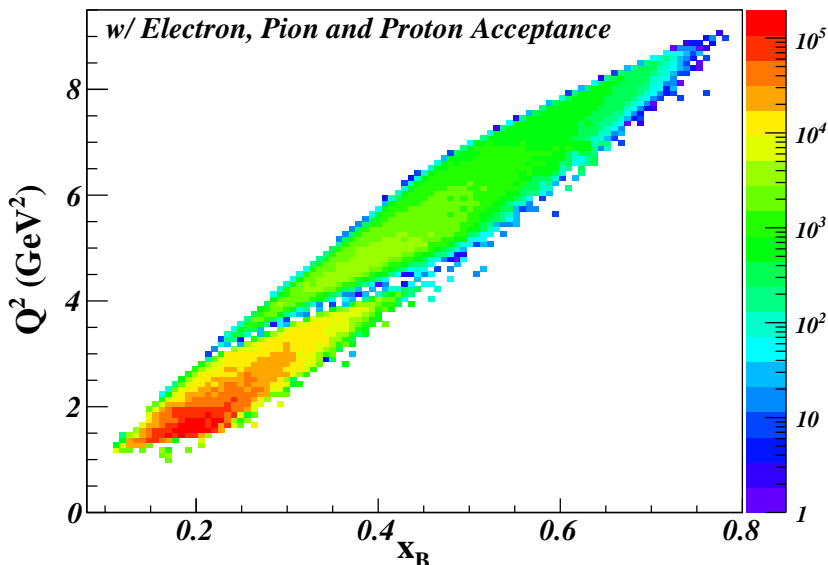


Figure 14: The triple coincidence $e+\pi^-+p$ kinematic coverage of DEMP events at 11 GeV within the SoLID acceptance. A $W > 2$ GeV cut is applied.

The kinematic coverage in Q^2 vs. x_B is shown in Fig. 14, using the existing SoLID detectors to detect electrons, pions and protons at $8^\circ \sim 24^\circ$. These distributions were weighted by the DEMP unpolarized cross sections and the SoLID acceptance profiles for electrons, pions and protons. A $W > 2$ GeV cut was also applied to exclude non-DIS events.

Fig. 15 shows the momentum and angular acceptance of π^- , electrons and protons which form the DEMP events and can be detected with the SoLID detectors. The recoil protons shown in Fig. 15 have low momenta ranging from 0.3 GeV/c up to 1.5 GeV/c, and are distributed in both the large- and forward-angle regions. The panels have applied cuts of $Q^2 > 4$ GeV 2 and $W > 2$ GeV, corresponding to the region of greatest physics interest.

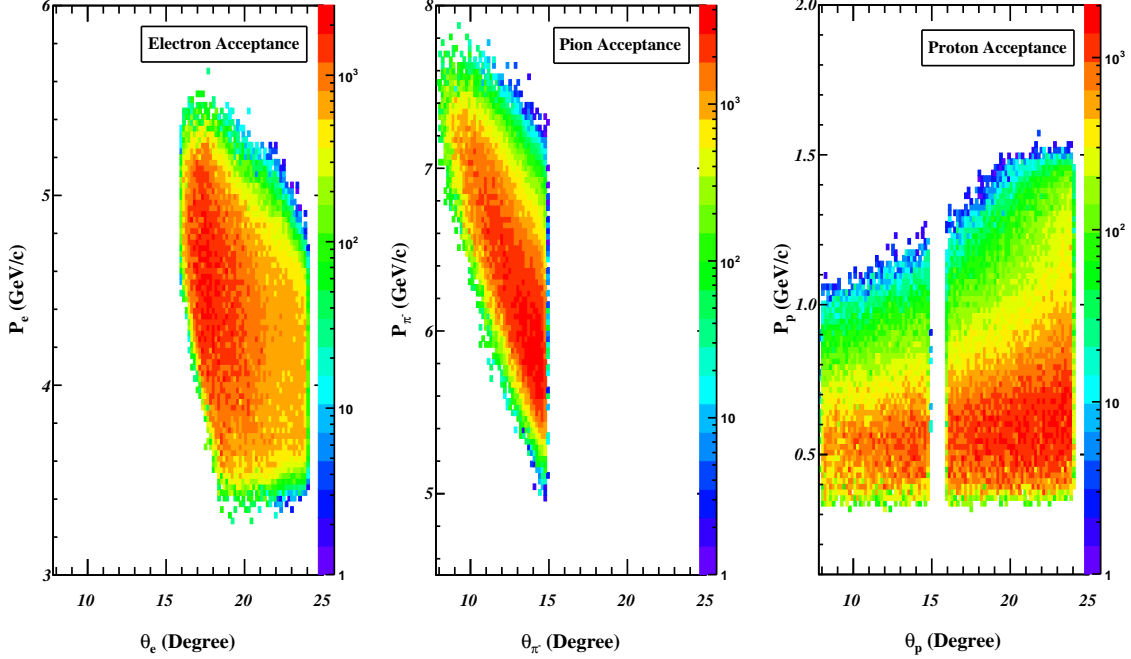


Figure 15: The acceptance of the momenta and polar angles for electrons, π^- and protons, respectively. Cuts of $Q^2 > 4 \text{ GeV}^2$ and $W > 2 \text{ GeV}$ are applied.

3.2 Estimated Rates

$Q^2 > 1 \text{ GeV}^2$	$Q^2 > 4 \text{ GeV}^2$
DEMP: $\vec{n}(e, e' \pi^- p)$ Triple-Coincidence (Hz)	
4.95	0.40
SIDIS: $\vec{n}(e, e' \pi^-) X$ Double-Coincidence (Hz)	
1424.62	35.77

Table 3: Triple-Coincidence rates for DEMP events compared with the SIDIS rates. A $W > 2 \text{ GeV}$ cut was applied. The online production trigger will be the SIDIS double-coincidence trigger of which rates are also given.

Table 3 lists the triple-coincidence rate of the DEMP events. The rates were calculated with the simulated events weighted by the target luminosity, the SoLID acceptances and unpolarized cross sections. The “raw” rates are not corrected by the beam and target polarization, target dilution and so on. Our conservatively estimated rate is around 4.95 Hz at $Q^2 > 1 \text{ GeV}^2$, or 0.40 Hz at $Q^2 > 4 \text{ GeV}^2$. For comparison, the table also gives the SIDIS rate which will be the online production trigger rate and is the main background of DEMP events.

3.3 Asymmetry Projections

The proposed experiment will run in parallel with E12-10-006, which has already been approved to run 48 days at $E_0=11 \text{ GeV}$. As shown in Fig. 16, we defined 7 $-t$ bins of which the boundaries are defined by the

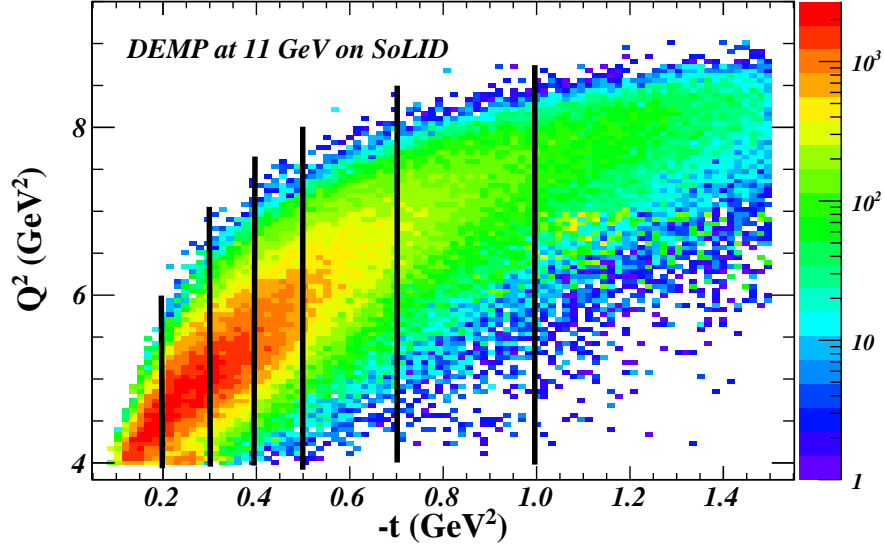


Figure 16: Q^2 vs. $-t$ coverage of triple coincidence $e+\pi^-+p$ DEMP events, where the black dashed lines specify the boundaries of 7 $-t$ bins. $Q^2 > 4$ GeV 2 and $W > 2$ GeV cuts are applied.

array:

$$-t[8] = [0.05, 0.20, 0.30, 0.40, 0.50, 0.70, 1.0, 3.0] \quad (\text{in GeV}^2) \quad (12)$$

The number of events ($N_i^{\uparrow\downarrow}$) in the i^{th} bin is calculated from the total simulated events after applying cuts on important kinematic variables, e.g. $Q^2 > 4$ GeV 2 , $W > 2$ GeV, $0.55 < \epsilon < 0.75$ and $-t_{\text{min}} < -t < -t_{\text{max}}$. Two simulated data sets with target polarization up and down follow exactly the same cuts and binning. As shown in Eqn. 13, each event surviving the cuts is then weighted by the polarized cross section, together with the acceptance of the electron, pion and proton. $N_i^{\uparrow\downarrow}$ is further corrected by the phase-space factor (PSF) defined in the event generator, the total number of randomly generated events (N_{gen}), beam-time (T), the target luminosity ($L = 10^{36}$ cm $^{-2}$ s $^{-1}$), and the overall detector efficiency (ϵ_{eff}):

$$N_i^{\uparrow\downarrow} = \left(\sum_{j \in i\text{-bin}} \sigma_j^{\uparrow\downarrow} \cdot A_j^e \cdot A_j^{\pi^-} \cdot A_j^p \right) \cdot (PSF/N_{\text{gen}}) \cdot T \cdot L \cdot \epsilon_{\text{eff}}, \quad (13)$$

where j is the j^{th} event in the i^{th} bin, $\sigma_j^{\uparrow\downarrow}$ is the cross section of the j^{th} event with the target polarization up or down. $A_j^{e(\pi^-,p)}$ is the acceptance weight of the electron (pion, proton) in this event. The detector efficiency, ϵ_{eff} , is approximately fixed at 85% as was used in the SIDIS proposals. $N_i^{\uparrow\downarrow}$ corresponds to the raw experimental count of electrons scattering on neutrons in ^3He after taking into account the target polarization ($P \sim 60\%$), the effective polarization of neutrons ($\eta_n \sim 0.865$), and the dilution effect from other reaction channels when electrons scatter on ^3He ($d \sim 0.9$).

With the numbers of simulated events in each bin for two anti-parallel target polarizations, one is able to reconstruct the average target single-spin asymmetry in that bin, which is identical to the experimental extracted asymmetry:

$$\langle A_{UT} \rangle = \frac{1}{P \cdot \eta_n \cdot d} \frac{N^\uparrow - N^\downarrow}{N^\uparrow + N^\downarrow}. \quad (14)$$

The statistical error of the target single spin asymmetry (A_{UT}) in each bin can be given as:

$$\delta A_{UT} = \frac{1}{P \cdot \eta_n \cdot d} \sqrt{\frac{1 - (P \cdot \langle A_{UT} \rangle)^2}{N_i^\uparrow + N_i^\downarrow}}, \quad (15)$$

As shown in Eqn. 9 of Sec. 1.4, A_{UT} can be further decomposed into six asymmetries with different azimuthal angular modulations:

$$\begin{aligned} A_{UT}(\phi, \phi_S) &= A_{UT}^{\sin(\phi - \phi_S)} \sin(\phi - \phi_S) + A_{UT}^{\sin(\phi_S)} \sin(\phi_S) \\ &+ A_{UT}^{\sin(2\phi - \phi_S)} \sin(2\phi - \phi_S) + A_{UT}^{\sin(3\phi - \phi_S)} \sin(3\phi - \phi_S) \\ &+ A_{UT}^{\sin(\phi + \phi_S)} \sin(\phi + \phi_S) + A_{UT}^{\sin(2\phi + \phi_S)} \sin(2\phi + \phi_S). \end{aligned} \quad (16)$$

In our generator, the first five different azimuthal modulations of A_{UT} are predicted with a phenomenological model as discussed in Appendix-A, and the last modulation is fixed to be zero as the model predicts a negligible asymmetry. As discussed in Sec. 1, two modulations, $A_{UT}^{\sin(\phi - \phi_S)}$ and $A_{UT}^{\sin(\phi_S)}$, are particularly interesting and are the main quantities this proposal aims to measure.

To demonstrate that the proposed measurement has the capability of extracting these asymmetries, we adopted the procedure presented in Ref. [22] to extract all five asymmetries by using a unbinned maximum likelihood (UML) method. Compared with the regular extraction methods, where the data in each $-t$ bin are further binned into two dimensional (ϕ, ϕ_S) bins, the UML method can perform much better fitting when the statistics are limited.

The polarized cross sections with two target polarization directions are given approximately by:

$$\sigma_\uparrow = \sigma_{UT}(\phi, \phi_S) = \left[1 + \frac{|P_T|}{\sqrt{1 - \sin^2(\theta_q) \sin^2(\phi_S)}} A_{UT}(\phi, \phi_S)\right] \cdot \sigma_{UU}(\phi) \quad (17)$$

$$\sigma_\downarrow = \sigma_{UT}(\phi, \phi_S + \pi) = \left[1 - \frac{|P_T|}{\sqrt{1 - \sin^2(\theta_q) \sin^2(\phi_S)}} A_{UT}(\phi, \phi_S)\right] \cdot \sigma_{UU}(\phi). \quad (18)$$

where $|P_T| = P \cdot \eta_n \cdot d$. Hence, the probability density function can be constructed as:

$$f_{\uparrow\downarrow}(\phi, \phi_S; \theta_k) = \frac{1}{C_{\uparrow\downarrow}} \left[1 \pm \frac{|P_T|}{\sqrt{1 - \sin^2(\theta_q) \sin^2(\phi_S)}} \sum_{k=1}^5 \theta_k \sin(\mu\phi + \lambda\phi_S)\right], \quad (19)$$

where θ_k , $k = 1 - 5$, are the values of asymmetries that can maximize the likelihood function. $C_{\uparrow\downarrow}$ is a normalization constant and is set to one as it is not important in the UML fitting. Here, we have dropped out the sixth asymmetry, which is zero. The UML function can be defined as:

$$L(\theta_k) = L_\uparrow(\theta_k) \cdot L_\downarrow(\theta_k) = \prod_{l=1}^{N_{MC}^\uparrow} [f_\uparrow(\phi_l, \phi_{S,l}; \theta_k)]^{w_l^\uparrow} \cdot \prod_{m=1}^{N_{MC}^\downarrow} [f_\downarrow(\phi_m, \phi_{S,m}; \theta_k)]^{w_m^\downarrow}. \quad (20)$$

where $w_l^\uparrow = \sigma_l^\uparrow \cdot A_l^e \cdot A_l^{\pi^-} \cdot A_l^p \cdot PSF/N_{gen} \cdot T \cdot L \cdot \epsilon_{eff}$, is the weight of the l^{th} simulated event. It takes into account the fact that the Monte-Carlo events are generated uniformly, and it also includes the experimental conditions, such as the acceptances of three particles and the detector efficiencies. For the real experimental data, the weight will only takes into account the acceptance correction, detector efficiencies correction and other experimental related corrections. From Eq. 13, one has $N_i^\uparrow = (\sum_{l \in i-bin} w_l^\uparrow)$. Note that

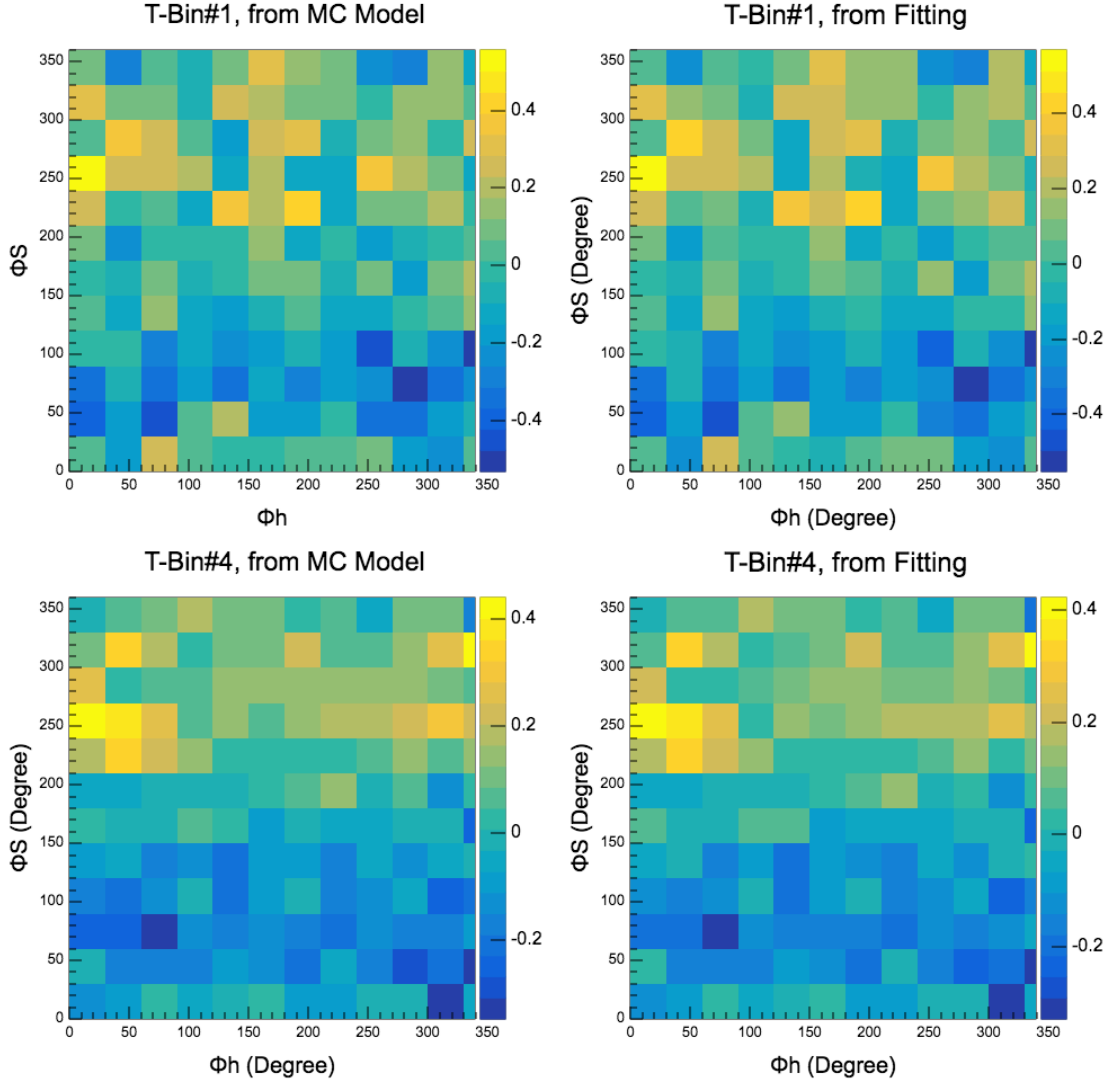


Figure 17: As an illustration of the validity of the asymmetry fitting method, the A_{UT} asymmetries of Eqn. 14 binned as a 2-dimensional scatter plot for 12×12 (ϕ, ϕ_S) bins, where dark (bright) color indicates negative (positive) single-spin asymmetry for that bin. *Left:* Average input model values per bin (Eqn. 16), *Right:* Average fit values from the UML analysis. Note, the UML analysis uses the full power of the data, without binning, as explained in the text.

$N_{MC}^\dagger = (\sum_{l \in i\text{-bin}})$ is simply the total number of simulated events in the i^{th} $-t$ bin without any weighting. In practice, we use the TMinuite package to minimize the following negative log-likelihood function:

$$-\ln L(\theta_k) = -\ln L_\uparrow(\theta_k) - \ln L_\downarrow(\theta_k) = -\sum_{l=1}^{N_{MC}^\dagger} w_l^\dagger \cdot \ln f_\uparrow(\phi_l, \phi_{S,l}; \theta_k) - \sum_{m=1}^{N_{MC}^\dagger} w_m^\downarrow \cdot \ln f_\downarrow(\phi_m, \phi_{S,m}; \theta_k). \quad (21)$$

Fig. 17 compares the distribution of A_{UT} vs. (ϕ, ϕ_S) from the UML fitting (right) to the direct statistical averaged model calculations (left). The variations in intensity from left to right and top to bottom of each panel indicate the presence of the different $\sin(\mu\phi + \lambda\phi_S)$ azimuthal modulations in the single-spin asymmetry. The $\sin(\phi_S)$ asymmetry is the only one not required to vanish at $-t_{min}$, giving a simple top-

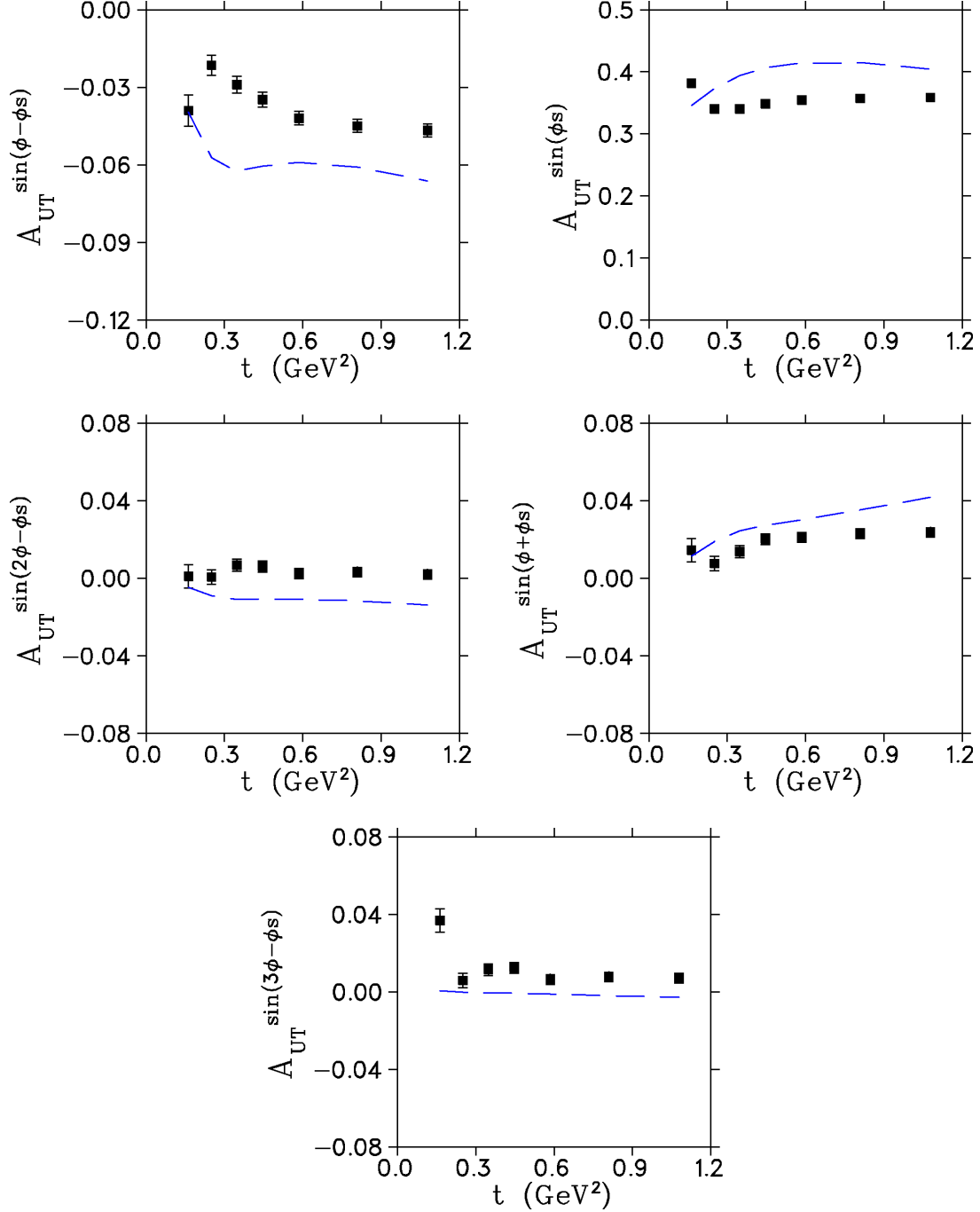


Figure 18: Projected uncertainties of the five single-spin asymmetry azimuthal modulations $A_{UT}^{\sin(\mu\phi + \lambda\phi_S)}$, as determined in the UML analysis, as a function of $-t$. The black squares are the extracted values for each bin, while the blue curves are the input values, as obtained from the model of Fig. 10 but averaged over the Q^2 acceptance of each bin. The simulated data include all radiative, Fermi, multiple scattering and energy loss effects. The difference between the input and output values is largely due to Fermi momentum, as discussed further in Sec. 4.5.

bottom modulation in the top panels (lowest $-t$ bin). In contrast, the fourth t -bin displays a additional modulation structure reflecting primarily the contributions of the $\sin(\phi - \phi_S)$ and $\sin(\phi + \phi_S)$ Fourier

components. The similarity between the left and right panels for both t -bins is readily apparent, confirming the validity of the fitting procedure. The equivalent HERMES figure, with lower statistics and coarser binning, can be found in Ref. [22].

Fig. 18 presents our expected precision for the five $A_{UT}(\phi, \phi_S)$ Fourier components extracted from the UML analysis vs. $-t$. Compared with the existing HERMES results (Fig. 11), the new measurement can provide more precision data to be directly compared with theoretical predictions. The detailed information for the two asymmetries of main interest are listed in Table 4.

t -bin	$\langle -t \rangle$	$\langle Q^2 \rangle$	$\langle x_B \rangle$	$A_{UT}^{\sin(\phi-\phi_S)}$	$\delta A_{UT}^{\sin(\phi-\phi_S)}$	$A_{UT}^{\sin(\phi_S)}$	$\delta A_{UT}^{\sin(\phi_S)}$
1	0.1625	4.378	0.3368	-0.0390	0.0060	0.3817	0.0059
2	0.2504	4.843	0.3886	-0.0214	0.0038	0.3399	0.0038
3	0.3478	5.301	0.4332	-0.0289	0.0031	0.3403	0.0031
4	0.4463	5.770	0.4711	-0.0347	0.0028	0.3484	0.0028
5	0.5854	6.324	0.5140	-0.0419	0.0026	0.3543	0.0025
6	0.8091	6.856	0.5595	-0.0449	0.0025	0.3570	0.0024
7	1.0783	7.002	0.5844	-0.0466	0.0025	0.3585	0.0024

Table 4: Detailed information of projected bins from the new DEMP measurements with SoLID. $\langle Q^2 \rangle$ and $\langle -t \rangle$ are in units of GeV^2 . The values are as obtained in the UML analysis, projected uncertainties are statistical only.

3.4 Missing Mass and Background

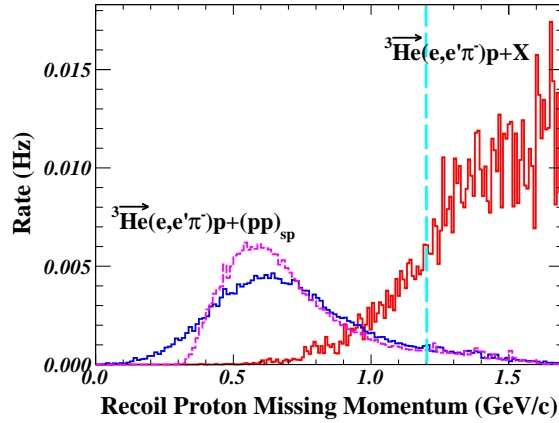


Figure 19: Missing momentum spectra of recoil protons in DEMP (blue) and SIDIS (red) processes with a polarized ${}^3\text{He}$ target. The dashed magenta curve is the DEMP missing mass only considering the Fermi motion, multiple scattering and the energy loss, while the blue and red curves have further taken into account the detector resolutions. The light-blue dashed line indicates a cut at $P_{miss} < 1.2 \text{ GeV}/c$ to remove most of the SIDIS events. Note that the SIDIS background is overestimated since we assume all SIDIS events contain protons in the final state.

In the DEMP reaction on a neutron, all three charged particles in the final state, e^- , π^- and p , can be cleanly measured by the SoLID detector system. Hence, contamination from other reactions, including DEMP with other two protons in ${}^3\text{He}$, can be greatly eliminated. The dominant background of the DEMP

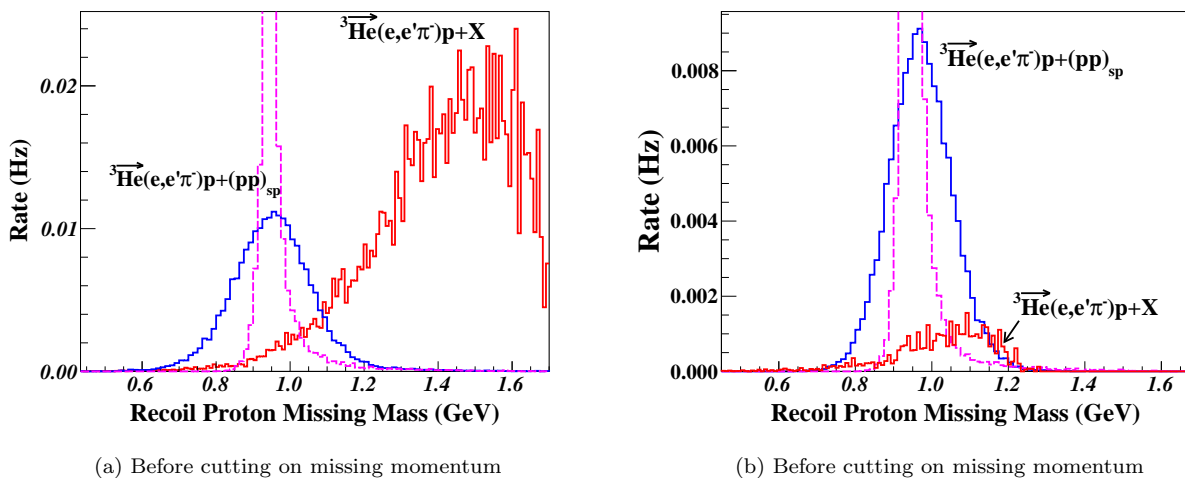


Figure 20: Missing mass spectra of recoil protons in DEMP (blue) and SIDIS (red) processes with a polarized ${}^3\text{He}$ target. The left (right) plot shows the background contamination from SIDIS events before (after) the missing momentum cut (shown in Fig. 19). The dashed magenta curve is the DEMP missing mass only considering the Fermi motion, multiple scattering and the energy loss, while the blue and red curves have further taken into account the detector resolutions. Note that the SIDIS background is overestimated, since we assume all SIDIS events contain protons in the final state.

measurement comes from the SIDIS reactions of electrons scattering on the neutron and two protons in ${}^3\text{He}$. In a SIDIS event, besides the scattered electron and the hadron (π^\pm , K^\pm etc.), there could be at least a proton in the target fragments, and in that case, the SIDIS event will be possibly misidentified as a DEMP event. In addition to identifying the recoil protons, which should largely suppress most of background, we will also rely on reconstructing the missing masses and missing momentum spectra of recoil protons to ensure the exclusivity of the DEMP events.

To calculate the missing mass and missing momentum of the recoil proton, we reconstructed the four-momentum Lorentz vectors of the incoming electron, the scattered electron and the pion. We assumed the neutron target is at rest even though its Fermi motion was simulated in the generator. We then used the momentum and energy conservation laws to calculate the missing mass and missing momentum of the recoil proton. Note that the energy loss, multiple scattering effects, and the detector resolutions have been considered in our study. Based on the current tracking study, the SoLID-SIDIS system can provide a momentum resolution of $2\%/\sqrt{E}$, a polar angle resolution of 0.6 mrad, an azimuthal angle resolution of 5 mrad and a vertex target position of 0.5 cm. In this measurement, we have conservatively proposed to only identify the recoil proton. However, with improved time resolution and certain tracking information, the momenta of the recoil protons will still be determined with certain accuracies, which gives us room to further suppress any background.

The SIDIS events, $p(e, e'\pi^-)X$ and $n(e, e'\pi^-)X$, were simulated with the same generator used for the SoLID-SIDIS proposals. The same acceptance profiles of scattered electrons and pions in DEMP were applied to the SIDIS events, along with the same kinematic cuts, such as $Q^2 > 4 \text{ GeV}^2$. It is difficult to estimate what percentage of the target fragments in SIDIS contain at least a proton, so we have to assumed all target fragments (“ X ”) contain proton. Such an assumption likely results in the SIDIS background being

significantly overestimated.

We followed exactly the same methods as used in DEMP to calculate the missing masses and missing momenta of the recoil protons in SIDIS. Fig. 19 shows the reconstructed missing momenta of both processes. One immediately sees that the main peak of the DEMP missing momentum spectrum is well separated from the SIDIS background, which can be largely rejected with a loose cut of $P_{miss} < 1.2$ GeV/c.

Fig. 20 shows the reconstructed missing mass spectra of the DEMP and SIDIS events w/ and w/o the missing momentum cuts. Before applying the missing momentum cut, the tail of the SIDIS background significantly leaks into the DEMP peak. Of course, keep in mind that the SIDIS rate is likely overestimated. After applying the missing momentum cut, the SIDIS background is largely suppressed. The total integrated SIDIS becomes 0.04 Hz, compared with the DEMP rate of 0.5 Hz. Further considering the fact that only a fraction “ X ” in SIDIS contains a proton, we conclude that the SIDIS background is negligible after the cut.

The background sources, such as the random coincident background events, will show up in the missing mass spectrum with more uniform distributions. We should be able to suppress most of them with tight missing momentum and missing mass cuts. The residual background events will be largely suppressed or corrected during the real asymmetry extraction. In general, we expect to have a clean measurement of the DEMP process because all of the final particles being detected.

3.5 Systematic Uncertainties

Sources	Relative Value
Beam Polarization	2%
Target Polarization	3%
Dilution Factor	1%
Nuclear Effect	< 4%
Acceptance	3%
Radiation Correction	2%
Background Contamination	< 5%

Table 5: Expected systematic errors.

The systematic errors are expected to be close to those given in the E12-10-006 proposal [1], as well as in other SIDIS experiments with SoLID [27, 28, 30, 31]. The procedure of extracting DEMP asymmetries is also expected to be similar to the SIDIS asymmetry extraction. The contamination of background should be well controlled by the proton detection and cuts on missing momenta and mass. However, to be conservative, we quote the overall systematic errors of background contamination to be 5% level. Here we list several major sources of systematic uncertainties as shown in Table 5.

4 Responses to Items Identified in the 2016 Review

Our 2016 SoLID Run-Group proposal was deemed to be of high scientific merit, but there were a number of technical questions that were asked to be studied before final approval can be given. The following list is compiled from the TAC, Theory, and SoLID review reports, reordered according to topic. Our response to each item is also given.

4.1 SoLID Acceptance Simulations

[TAC] *The simulations for this measurement may benefit from tracking DEMP events through the full SoLID GEANT4 simulation (GEMC), particularly for kinematics with the lowest momentum protons (300 MeV/c).*

GEMC is a GEANT4-based simulation framework designed mainly for CLAS12. SoLID has adopted this framework to do some preliminary studies, but implementation of a realistic SoLID detector information is still underway. To address this comment, we have used our generator in two different types of simulations. The projected results in Secs. 3.2, 3.3 incorporate electron radiation, multiple scattering and ionization energy loss in the generator. Then, for every detected particle in each event, we smeared the momenta and angles of the final state particles by the detector resolutions based on the SoLID tracking study, and then used the acceptance profiles obtained with the SoLID-SIDIS GEMC simulation.

In the second study, the event generator creates a LUND-format file for the three outgoing particles, e^- , π^- , p . We can store up to eight variables (Q^2 , $-t$, W , etc.) in the header lines of the LUND file. Events are generated with bremsstrahlung and multiple scattering for the incoming electron and Fermi motion of the target neutron. Events are generated uniformly over the 40 cm length of the SIDIS ^3He target and a 25 mm \times 25 mm raster size is assumed. Particle acceptance is studied with the SoLID SIDIS GEMC configuration, incorporating multiple scattering and energy loss, as well as the individual detector apertures via the GEANT4 framework. The GEMC flux tree is used to see if a particle hits a specific detector.

In this second study, a DEMP event is defined as the following ‘trigger’:

$$\text{DEMP Event:} = T_{LA+FA}^{e'} \text{ and } T_{FA}^{\pi^-} \text{ and } T_{LA+FA}^p,$$

where

- $T_{LA+FA}^{e'}$ is true if an electron hits the virtual planes of (LGC and HGC and FAEC) or LAEC,
- $T_{FA}^{\pi^-}$ is true if a pion hits the virtual planes of HGC and FAEC and MRPC,
- T_{LA+FA}^p is true if a proton hits the virtual planes of (MRPC and FASPD) or LASPD.

Fig. 21 shows the acceptances for all three particles when an event passes these DEMP event triple-coincidence conditions. As expected, the results strongly resemble those obtained in the first study (Fig. 15), with the low momentum proton acceptance now being more accurately modeled. Because the DEMP process has a very low physics rate, and it takes a huge amount of computer time to accumulate enough statistics, some regions have stronger statistical fluctuation effects. However, the experimental requirement of detecting protons is more relaxed compared with the detection of electrons and pions, simply because we only rely on the Time-of-Flight information to separate protons from other positive particles. We intend to perform

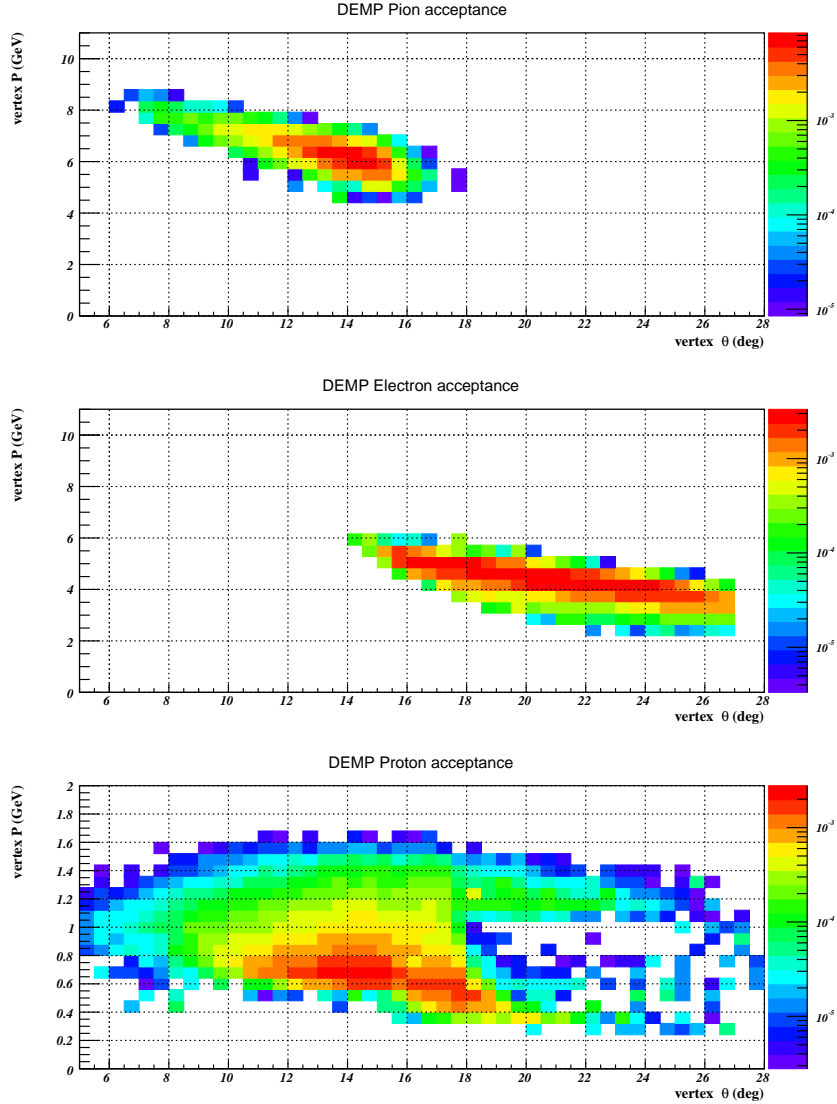


Figure 21: The triple coincidence $e+\pi^-+p$ acceptance of the momenta and scattering angles for electrons, π^- and protons for DEMP events as simulated by GEMC. $Q^2 > 4 \text{ GeV}^2$ and $W > 2 \text{ GeV}$ cuts are applied. The plotted kinematic quantities are the emitted particle values in the lab frame.

a more careful study of reconstructing low momentum protons, but we believe the SoLID detector systems will have good coverage of detecting protons.

It is important to note that the angles plotted in Fig. 15 are in the detector frame, while those in Fig. 21 correspond to the reaction vertex location within the simulated target volume for that event. This causes the gap between the FA and LA angular acceptances to be largely blurred out, as well as a slight enlargement of the accepted angular range. Similarly, the plotted momenta are the emitted particle values, not the detected values, corresponding to what would be obtained in the data analysis after correcting for energy loss. In comparison to the first study, this difference in plotting variables causes the lower range of the detected proton momentum to appear to have shifted upward slightly, to 300-350 MeV/c. The overall

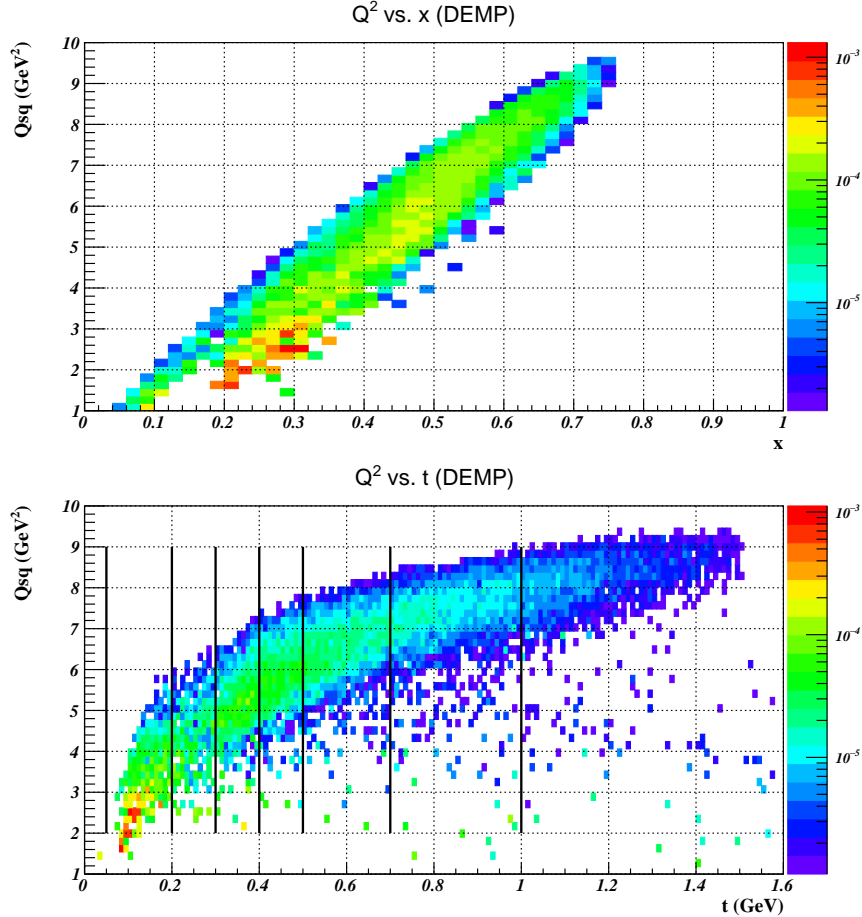


Figure 22: Q^2 vs. x and $-t$ coverages of triple coincidence $e+\pi^-+p$ DEMP events as simulated by GEMC, where the black dashed lines specify the boundaries of 7 $-t$ bins. A $W > 2$ GeV cut is applied.

triple-coincidence rate and accepted t -range are only marginally affected.

Fig. 22 is also the result of GEMC simulations, using the same triple coincidence trigger conditions. The close resemblance to Figs. 14, 16 is clear. Finally, because there were some oral questions about the W' acceptance, we show both the W' and W coverages versus x in Fig. 23. Since we only tag the proton and don't anticipate an accurate value for its' momentum, we compute W' (the invariant mass of the undetected hadrons) analogous to how we compute P_{miss} and M_{miss} (i.e. assuming the only detected hadron is the π^-). This also keeps the definition of W' to be exactly the same as was defined for SIDIS, for comparison. As expected for an exclusive reaction, W' is sharply peaked at the mass of the recoil proton, with a sparsely populated tail due to nuclear effects. In contrast, the SIDIS events are distributed over a broad range $1.5 < W' < 3.5$ GeV [1].

We would like to stress that the SoLID simulation tool is still under massive development, and the detector designs still need to be finalized. The above results should only be considered to be preliminary. Together with the other approved physics programs using SoLID, we plan to perform more careful study when the SoLID detector designs are completed and the full simulation software is available.

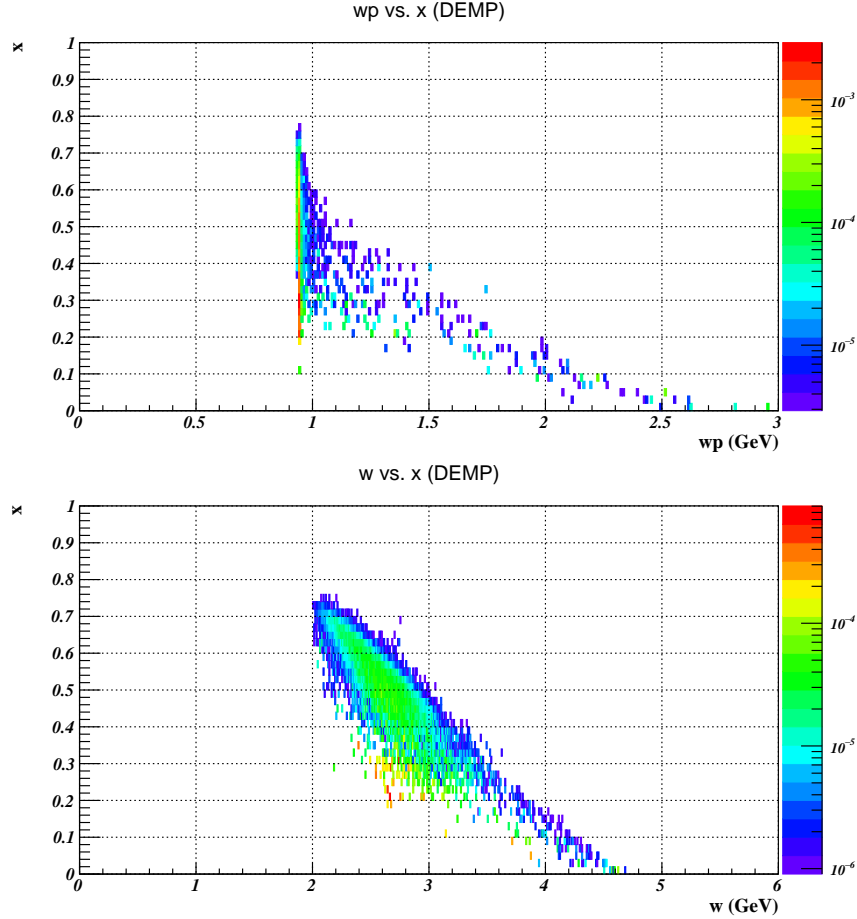


Figure 23: *Top*: W' vs. x coverage, *Bottom*: W vs. x coverage of triple coincidence $e+\pi^-+p$ DEMP events as simulated by GEMC. A $W > 2$ GeV cut is applied.

4.2 Experimental Background

[SoLID] *The committee is convinced that the SIDIS background is likely not a major problem. However, an alternate approach (rather than SIDIS fragmentation functions) could be used. The primary background channel under study is ${}^3\text{He}(e, e'\pi^-)pp$ with the two undetected protons as spectators. The continuum background that can leak under the quasi-exclusive peak can be of the form $e + n \rightarrow e' + \pi^- + \Delta^+$ with the Δ^+ decaying to $p + \pi^0$.*

[Theory] *The authors may want, however, to expand on possible contamination arising from Δ^{++} production on bound protons, and subsequent decay into π^+ and p .*

We take this comment to mean the $e + p \rightarrow e' + \pi^- + \Delta^{++}$ background reaction, as otherwise there is no π^- in the final state to satisfy the offline event finder.

Neither $\pi^- \Delta$ final state is expected to be a substantial source of contamination. We have investigated and compared the kinematics of the $\pi^- n$ and $\pi^- \Delta$ final states. The missing momentum of the $\pi^- \Delta$ state

is about 500 MeV/c higher than the π^-n final state, very similar to the difference between the DEMP and SIDIS distributions in Fig. 19. A cut at 1.2 GeV/c missing momentum will discriminate against $\pi^- \Delta$ events. In addition, the $\pi^- \Delta$ final state is centered about 300 MeV higher in missing mass than the π^-n state, and will be further suppressed by a cut of approximately $M_{miss} < 1.05$ GeV. We estimate the $\pi^- \Delta$ contamination remaining after the application of both cuts to be very similar to that already shown in Fig. 20.

4.3 Resolution and Energy Loss

[SoLID] The effects of Fermi-smearing, detector resolution, ionization energy loss and bremsstrahlung need to be clarified. Although they seem to all be included in Figs. 15 and 16, it was not clear which curves included which effects.

We have revised the text to make this more clear. All of the results shown incorporate all these effects.

4.4 Projected Uncertainties

[SoLID] The extraction of the term $|\sigma_{TT}^y + 2\epsilon\sigma_L^y|$ in Eqn. 8 from the other $\sin\beta$ and $\cos\beta$ terms requires good knowledge of the β -acceptance in each t -bin. This should be shown, in addition to the acceptance plots of Fig. 12.

We have put much more effort into understanding the (ϕ, ϕ_S) coverage of each t -bin, and we hope the proposal more clearly addresses both the goals of the experiment and the potential limitations. As presented in Sec. 3.3, we have used the same unbinned maximum likelihood (UML) analysis that was used by the HERMES Collaboration in the analysis of their experimental data. It is clear that the large azimuthal acceptance and high luminosity capabilities of the SoLID detector makes it very well suited to this measurement, and there should be no major obstacles to cleanly identify the desired $\sin(\phi - \phi_S)$ and $\sin(\phi_S)$ asymmetries.

The two limitations we face are the following:

- the effect of ^3He Fermi momentum. This is discussed more fully in Sec. 4.5.
- we are less likely to extract definitive values for the small and more rapidly varying $\sin(2\phi - \phi_S)$, $\sin(2\phi + \phi_S)$, $\sin(3\phi - \phi_S)$ asymmetries after all statistical and systematic uncertainties are included. However, we have shown that this should not adversely affect the main physics goals of our measurement.

We are confident that we can obtain a significant physics result should this proposal be accepted, and that this can help justify funding for the SoLID project as one of its flagship measurements.

[SoLID] The collaboration should attempt to quantify the projected precision of the measured spin-dependent cross section. Although the asymmetry may have a smaller error bar, the spin-dependent cross section difference has a simpler interpretation.

One of the biggest advantages of DEMP measurements with transversely polarized target is that the asymmetries can suffer many fewer higher twist effects than the cross sections. As shown in Fig. 5, higher

twist corrections, which are expected to be significant in Jefferson Lab kinematics, likely cancel in the formation of the single spin asymmetry, leading to a precocious scaling of A_L^\perp at moderate Q^2 [15, 18]. This is one of the reasons for the intense theoretical interest in these measurements.

Thus, while the extraction of the absolute spin-dependent cross sections will undoubtedly be helpful for confirming the theoretical interpretation of our results, they will be dominated by the higher twist effects. It is difficult to quantify the expected precision at this early stage, given that SoLID is not designed for absolute cross section measurements. To be conservative, this proposal only relies on the extraction of the azimuthal asymmetry components from the target up-down polarization difference, where many systematic uncertainties cancel. This can be done reliably, even if the systematic uncertainties are otherwise too large for reliable absolute cross section measurements. The quantitative estimate of detector efficiency and acceptance correction uncertainties, absolute kinematic offsets, etc. requires dramatically more study and a possible optimization of the SoLID detector system.

Ultimately, the measurement presented in this proposal is important preparatory work for future measurements at the EIC, where the higher twist contributions should be smaller. The Electron-Ion Collider is optimized for transverse single spin asymmetry measurements such as these, and the ability to have both polarized ^3He and proton beams will allow $A_{UT}^{\sin(\phi-\phi_s)}$ to be directly compared for the $\vec{n}(e, e'\pi^-)p$ and $\vec{p}(e, e'\pi^+)n$ reactions, without target dilution, over a broad kinematic range. In the meantime, the proposed measurement with SoLID is our best short-term opportunity to considerably advance over the pioneering HERMES data.

4.5 Fermi Momentum Effects

[SoLID] Fermi-momentum is not just a kinematic effect. It also affects the DEMP amplitude. The ^3He momentum distribution $\rho(p)$ is plotted in Fig. 10 (Appendix A). The weighted distribution $p^2\rho(p)$ peaks at $p_n \approx 60$ MeV/c. This means that the effective x_B is smeared by $\approx p_n/M \approx 6\%$. The significance of this effect should be discussed. Also, if the proton momentum resolution is good enough, it will be possible to correct for this effect, event-by-event.

[Theory] The authors may want to switch off ^3He Fermi motion in their simulations and determine how large and in which kinematics they see a difference. Having evidence of non-negligible nuclear effects at an early stage would encourage theorists to extend now their calculations from inclusive to exclusive measurements for a timely and correct utilization of the data the authors propose to take. It would also be helpful to elaborate on the possible corrections in addition to Fermi motion, such as from binding and nucleon off-shell effects, as well as corrections beyond the impulse approximation from rescattering or final state interactions of the detected proton.

We agree that if the proton momentum resolution is sufficiently good, it will be possible to correct for Fermi momentum on an event-by-event basis. We are familiar with this technique from our work with the A2 Collaboration at Mainz, for example. For the purposes of this proposal, we take the more pessimistic view that the proton resolution is likely not good enough to make this correction, even though the removal of the Fermi momentum affect would simplify the physics interpretation of our data and further increase its likely physics impact.

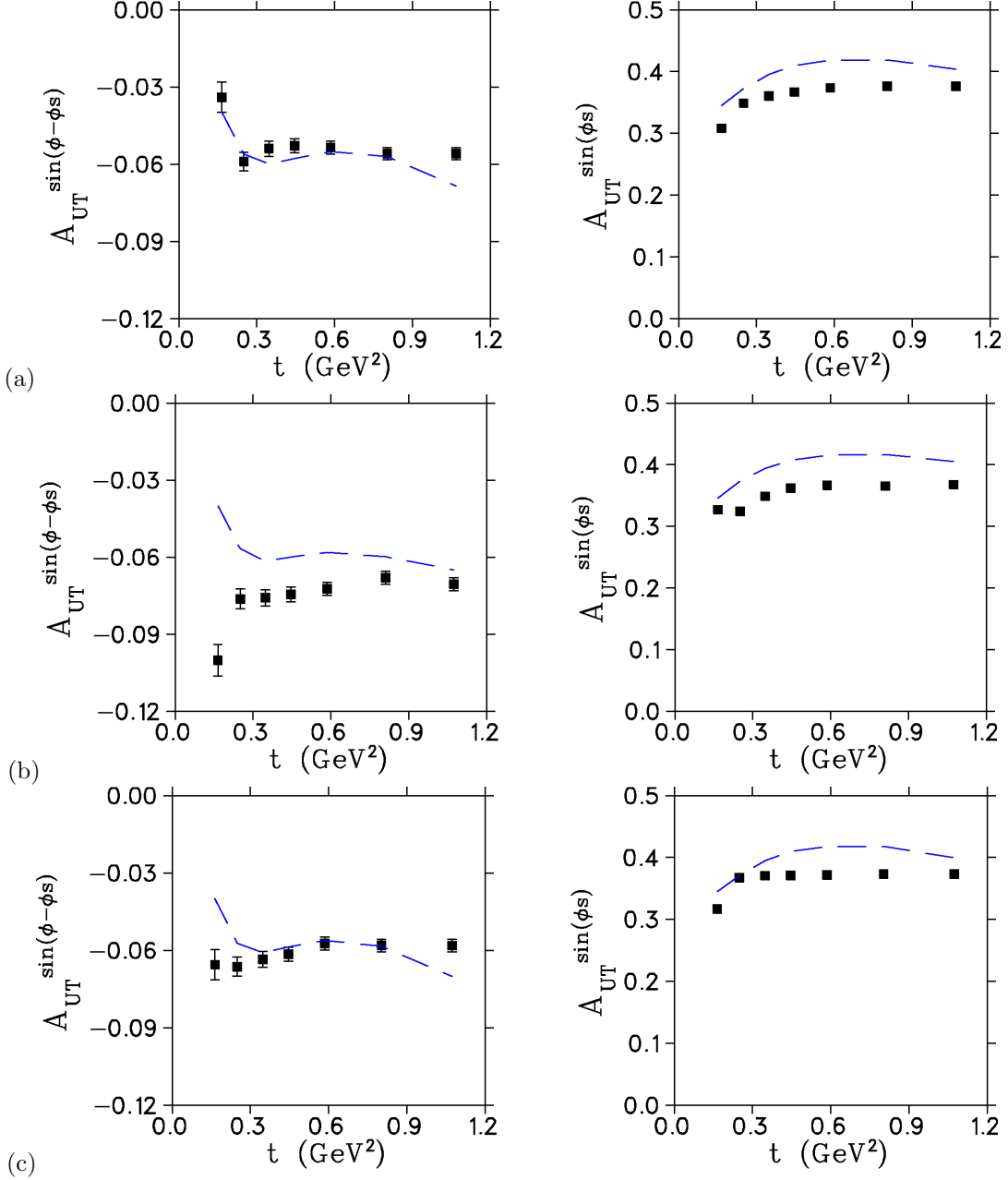


Figure 24: Projected values and uncertainties of the two dominant single-spin asymmetry modulations, $\sin(\phi - \phi_S)$ (left) and $\sin(\phi_S)$ (right) for the a) *simple*, b) *fermi* and c) *mult_nofermi* cases, as discussed in the text.

To get a better estimate of the impact of Fermi momentum, we have run the generator in a variety of configurations and repeated the analysis of Sec. 3.3. These configurations were:

- *simple*: All Fermi momentum, multiple scattering, energy loss effects turned off.
- *fermi*: Same as *simple* except that Fermi momentum is turned on. This allows the Fermi momentum effect to be isolated separate from other effects.

- *mult*: All Fermi momentum, multiple scattering, energy loss effects turned on. This is the default configuration, presented in Fig. 18.
- *mult_nofermi*: Same as *mult* except that Fermi momentum is turned off. This allows the anticipated effect of correcting Fermi momentum event-by-event, should the recoil proton momentum resolution be sufficiently good, to be modeled.

While all five modulations were fit in each case, only the two of physics interest are shown in Fig. 24. It is clearly seen in panel a) that the agreement between input and output values is very good when all Fermi momentum, scattering and energy loss effects are turned off. This validates our UML procedure. The effect of Fermi momentum can be seen by comparing panels b) and a), or alternately Fig 18 with panel c). The two comparisons are similar, giving rise to a deviation to the $\sin(\phi - \phi_S)$ asymmetry of about -0.02, and a deviation to the $\sin(\phi_S)$ asymmetry of about -0.04. Panel c) clearly shows that if we are able to correct the data for Fermi momentum on an event-by-event basis, it is in principle possible to remove most of this effect on the asymmetries, even in the presence of multiple scattering, resolution, and other smearing effects.

We hope this estimate of Fermi-momentum effects at an early stage will encourage theorists to extend their calculations for a timely and correct utilization of our proposed data, as suggested in the Theory review comment.

4.6 Dialog with Theorists

[SoLID] There are a number of important theory issues raised by this proposal. These probably cannot be fully resolved before re-submission, but it will be important to have a clear dialog with relevant theorists (and experimentalists) in place... Both Goloskokov and Kroll, and Liutti and Goldstein, have published estimates of σ_T , based on transversity GPDs and a twist-3 helicity-flip pion distribution amplitude. One or the other of these theory groups should be engaged in a discussion of both the $|\sigma_L^y|$ and $|\sigma_{TT}^y|$ terms.

We have been in communication with Goloskokov and Kroll on the physics objectives of this proposal for some years, and they provided helpful comments to our 2016 proposal. With the additional time we had available for the 2017 proposal, Goloskokov and Kroll generously provided new asymmetry calculations, based on their best estimates of σ_T , σ_{TT} for SoLID kinematics. We are confident that approval of this proposal will raise the interest of other theorists to the physics potential of our measurements, and we will have dialog with them.

[SoLID] The QCD factorization theorem implies color transparency for the final state π^- in this proposal. Thus the ${}^3\text{He}(e, e'\pi^-)$ final state interactions (FSI) are identical with ${}^3\text{He}(e, e'p)$, just with a more exotic scattering amplitude. It is not practical to obtain full FSI calculations before resubmission, but a dialog should be started both with the groups doing FSI calculations, and the groups doing Deep Virtual calculations on light nuclei. Empirically, it will be useful to determine if the FSI ‘peak’ lies within the ${}^3\text{He}(e, e'\pi^-p)pp$ acceptance of this proposal.

We have made some estimates of FSI effects, based on the empirical parameterization of πN differential cross sections discussed in Sec. A.6 of the Appendix. The results of our study indicate that the FSI ‘peak’

does not lie within the acceptance of this proposal and that FSI effects are expected to be small. Based on the πN differential cross sections and the fact that there are only two proton spectators in the final state, we anticipate only about 1% of events will suffer FSI interactions. The FSI fraction is weakly dependent on Q^2 , rising to about 1.2% for events with $Q^2 > 5 \text{ GeV}^2$ in our study. Of these, a large fraction of the FSI events are scattered outside the triple coincidence acceptance, reducing the FSI fraction to $\sim 0.4\%$. This will be further reduced by analysis cuts such as $P_{miss} < 1.2 \text{ GeV}/c$.

Over the longer term, we will consult with theoretical groups for a more definitive study of FSI effects. For example, Del Dotto, Kaptari, Pace, Salme and Scopetta recently published [39] a study of FSI effects in SIDIS from a transversely polarized ^3He target in SBS, SoLID and EIC kinematics. The SIDIS final state has more outgoing particles than DEMP, so there are more opportunities for FSI interactions there than the simple $\pi^- ppp$ final state considered here. Nonetheless, they were able to show that the extracted Sivers and Collins asymmetries are basically independent of FSI, evaluated within the generalized eikonal approximation and a realistic distorted spin-dependent spectral function. A similar calculation for DEMP, after this proposal is approved, would be a natural extension of their work.

5 Summary

The $A_{UT}^{\sin(\phi-\phi_s)}$ transverse single-spin asymmetry in the exclusive $\bar{n}(e, e'\pi^-)p$ reaction has been noted as being especially sensitive to the spin-flip generalized parton distribution (GPD) \tilde{E} . Factorization studies have indicated that precocious scaling is likely to set in at moderate $Q^2 \sim 2 - 4 \text{ GeV}^2$, as opposed to the absolute cross section, where scaling is not expected until $Q^2 > 10 \text{ GeV}^2$. This relatively low value of Q^2 for the expected onset of precocious scaling is important, because it is experimentally accessible at Jefferson Lab. As we have shown through a detailed UML analysis, the $A_{UT}^{\sin(\phi_s)}$ asymmetry can also be extracted from the same data, providing powerful additional GPD model constraints and insight into the role of transverse photon contributions at small $-t$.

This measurement is complementary to a proposal to measure the longitudinal photon, transverse nucleon, single-spin asymmetry A_L^\perp with the SHMS+HMS in Hall C [5]. The good resolution and reproducible systematic uncertainties of the SHMS+HMS setup allow the L-T separation needed to reliably measure this quantity. However, a wide $-t$ coverage is needed to obtain a good understanding of the asymmetry, and it always been intended to complement the SHMS+HMS A_L^\perp measurement with an unseparated $A_{UT}^{\sin(\phi-\phi_s)}$ measurement using a large solid angle detector. The high luminosity capabilities of SoLID make it well-suited for this measurement. Since an L-T separation is not possible with SoLID, the observed asymmetry is expected to be diluted by the ratio of the longitudinal cross section to the unseparated cross section. This was also true for the pioneering HERMES measurements, which provided valuable constraints to models for the \tilde{E} , \tilde{H} , and H_T GPDs.

In our proposal, we will analyze the E12-10-006 event files off-line to look for $e - \pi^- - p$ triple coincidence events in SoLID for the case where the recoil proton is emitted $8^\circ < \theta < 24^\circ$. To be conservative, we assume only that the recoil proton is identified, and its' momentum is not used to further reduce the SIDIS background. This study yields data that are a considerable advance over the HERMES measurement in terms of kinematic coverage and statistical precision. This measurement is also important preparatory work for future measurements at the EIC, which will allow $A_{UT}^{\sin(\phi-\phi_s)}$ to be directly compared for the $\bar{n}(e, e'\pi^-)p$ and $\bar{p}(e, e'\pi^+)n$ reactions over a broad kinematic range.

A Monte Carlo model of Deep Exclusive π^- Production from the Neutron in ^3He

The Monte Carlo studies needed for this proposal require a reaction model for an experimentally unexplored region of kinematics, at higher values of Q^2 , $-t$ and W than covered by existing data. This appendix describes the model and the constraints used.

A.1 Definition of the Cross Section and Single-Spin Asymmetries

The differential cross section for exclusive π production from the nucleon can be written as

$$\frac{d^5\sigma}{dE'd\Omega_{e'}d\Omega_\pi} = \Gamma_V \frac{d^2\sigma}{d\Omega_\pi}. \quad (22)$$

The virtual photon flux factor Γ_V is defined as

$$\Gamma_v = \frac{\alpha}{2\pi^2} \frac{E'}{E} \frac{K}{Q^2} \frac{1}{1-\epsilon}, \quad (23)$$

where α is the fine structure constant, K is the energy of real photon equal to the photon energy required to create a system with invariant mass equal to W and ϵ is the polarization of the virtual photon.

$$K = (W^2 - M_p^2)/(2M_p) \quad (24)$$

$$\epsilon = \left(1 + \frac{2|\mathbf{q}|^2}{Q^2} \tan^2 \frac{\theta_e}{2}\right)^{-1}, \quad (25)$$

where θ_e is the scattering angle of scattered electron.

The two-fold differential cross section $\frac{d^2\sigma}{d\Omega_\pi}$ in the lab frame can be expressed in terms of the invariant cross section in center of mass frame of the photon and nucleon,

$$\frac{d^2\sigma}{d\Omega_\pi} = J \frac{d^2\sigma}{dt d\phi}, \quad (26)$$

where J is the Jacobian of transformation of coordinates from lab Ω_π to t and ϕ (CM).

Following Ref. [22], we consider separately the unpolarized and polarized target contributions to the invariant photon nucleon cross section,

$$d\sigma = d\sigma_{UU} + d\sigma_{UT}. \quad (27)$$

In the one-photon exchange approximation, the unpolarized nucleon cross section for $n(e, e'\pi^-)p$ can be expressed in four terms. Two terms correspond to the polarization states of the virtual photon (L and T) and two states correspond to the interference of polarization states (LT and TT),

$$d\sigma_{UU} = \epsilon \frac{d\sigma_L}{dt} + \frac{d\sigma_T}{dt} + \sqrt{2\epsilon(\epsilon+1)} \frac{d\sigma_{LT}}{dt} \cos \phi + \epsilon \frac{d\sigma_{TT}}{dt} \cos 2\phi, \quad (28)$$

where ϕ is the angle between lepton plane and hadron plane (Fig. 3). The first two terms of Eqn. 28 correspond to the polarization states of the virtual photon (L and T) and last two terms correspond to the interference of polarization states (LT and TT). ϵ is the ratio of longitudinal to transverse virtual-photon fluxes

$$\epsilon = \left(1 + \frac{2|\mathbf{q}|^2}{Q^2} \tan^2 \frac{\theta_e}{2}\right)^{-1}. \quad (29)$$

The constraints used to parameterize $d\sigma_{UU}$ are described in Sec. A.2.

The additional contribution when the target nucleon is transversely polarized can be parameterized [3,22] as

$$d\sigma_{UT} = -\frac{P_T}{\sqrt{1 - \sin^2 \theta \sin^2 \phi_S}} \sum_{k=1}^6 \sin(\mu\phi + \lambda\phi_S) \Sigma_k, \quad (30)$$

where ϕ_S is angle between the target polarization and lepton planes (Fig. 3), the Σ_k are given by

$$\Sigma_k = A_{UT}^{\sin(\mu\phi + \lambda\phi_S)_k} \times d\sigma_{UU}(\phi), \quad (31)$$

and the $\sin(\mu\phi + \lambda\phi_S)$ are the different azimuthal modulations. The calculation of $d\sigma_{UT}$ in the event generator is described in Sec. A.3.

A.2 Cross Section Model for Higher Q^2 Kinematics

A.2.1 Constraints

All of the following data were used as constraints on the parameterizations used in this model:

- From Hall C, precise L/T separated experimental data of exclusive electroproduction of π^- on ^2H are available up to $Q^2 = 2.57 \text{ GeV}^2$, $-t = 0.350 \text{ GeV}^2$ and $W = 2.168 \text{ GeV}$ [34].
- Also from Hall C, precise L/T separated experimental data of exclusive electroproduction of π^+ on ^1H are available up to $Q^2 = 2.703 \text{ GeV}^2$, $-t = 0.365 \text{ GeV}^2$ and $W = 2.127 \text{ GeV}$ [25], and separated σ_L and σ_T are measured up to $Q^2 = 4.703 \text{ GeV}^2$ and $W = 2.2 \text{ GeV}$ [35] and [36].
- CLAS experiment E99-105 measured the unseparated exclusive π^+ cross section from ^1H at Q^2 up to 4.35 GeV^2 and $-t$ up to 4.5 GeV^2 [37].
- The HERMES collaboration measured the unseparated cross section for $Q^2=3.44 \text{ GeV}^2$ and 5.4 GeV^2 [38] at $W=4 \text{ GeV}$.

An additional constraint in our parameterization comes from the Vrancx-Ryckebusch (VR) model [40]. This is a Regge model with a parametrization of the deep inelastic scattering amplitude added to improve the description of σ_T . The description of σ_L in the model is constrained by a fit to the Hall C $p(e, e' \pi^+)n$ data from Ref. [25]. The model provides a good description of exclusive charged pion electroproduction above the resonance region. It has been checked for reliability against the Hall B and C data listed above, for $W > 2 \text{ GeV}$, Q^2 from 0.35 to 4.98 GeV^2 . The model is believed to be reliable for $-t \leq 0.5 \text{ GeV}^2$, but it overshoots the data for $-t > 0.5 \text{ GeV}^2$.

A.2.2 Parametrization of σ_L , σ_T , σ_{LT} , & σ_{TT}

For exclusive DEMP in SoLID, the kinematic region of interest for the parametrization of $\sigma_{L,T,LT,TT}$ is Q^2 from 4.0 GeV to 7.5 GeV^2 , $-t$ from $-t_{min}$ to 1.0 GeV^2 , and we set $W = 3.0 \text{ GeV}$. After the parametrization of $\sigma_{L,T,LT,TT}$ for $-t$ and Q^2 , we used the same W dependence given by [25], which is $(W^2 - M^2)^{-2}$ where M is the proton mass. Our parametrization of all four cross sections is given in equations 32 to 35.

$$\sigma_L = \exp(P_1(Q^2) + |t| * P'_1(Q^2)) + \exp(P_2(Q^2) + |t| * P'_2(Q^2)) \quad (32)$$

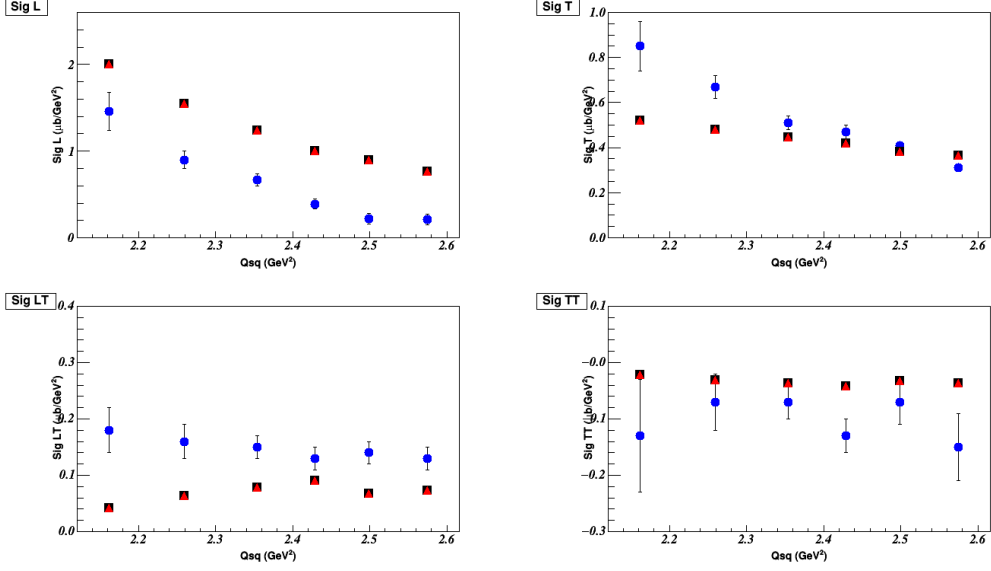


Figure 25: A comparison of last six points of table v of [34], the VR model, and our parametrization values vs. Q^2 for π^- electroproduction. Experimental data are shown in blue circles, the VR model is shown in red triangles, and our parametrization is shown in black boxes. In each graph, the value of $-t$ is decreasing left to right from a maximum value 0.35 GeV^2 to 0.15 GeV^2 . The value of W also decreases left to right from 2.2978 GeV to 2.1688 GeV .

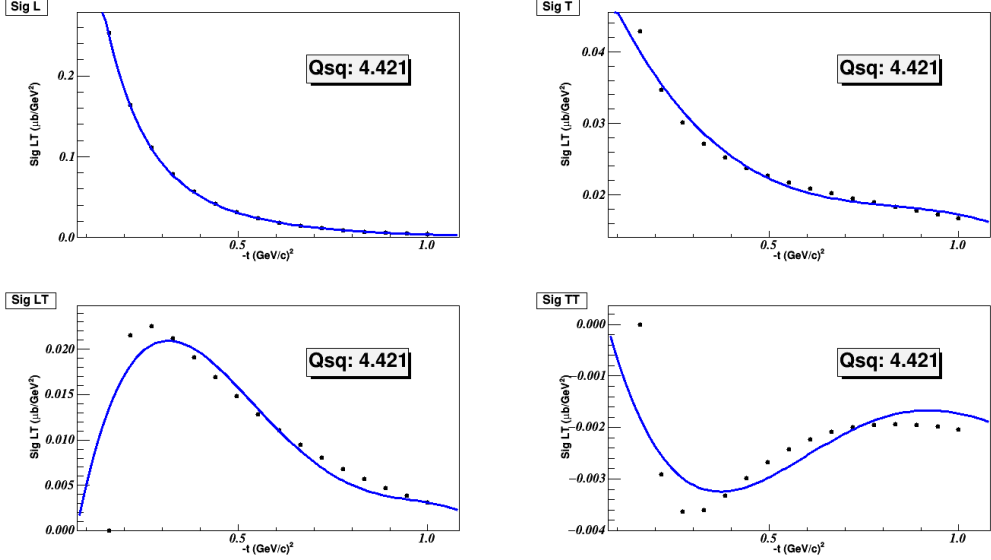


Figure 26: A comparison of parametrized $\sigma_{L,T,LT,TT}$ and VR model values at $Q^2 = 4.421 \text{ GeV}^2$ and $W = 3.0 \text{ GeV}$. Black points are VR model values and the blue line is the parametrized $\sigma_{L,T,LT,TT}$ given by equations 32 to 35.

$$\sigma_T = \frac{\exp(P_1(Q^2) + |t| * P'_1(Q^2))}{P_1(|t|)} \quad (33)$$

$$\sigma_{LT} = P_5(t(Q^2)) \quad (34)$$

$$\sigma_{TT} = P_5(t(Q^2)) \quad (35)$$

Here, the parameters P_i are polynomial functions of i^{th} order. Each coefficient (P_i) of the fifth order equations 34 and 35 is a further second order polynomial of Q^2 . Deep exclusive π^- events are generated using a C++ code. The quality of parametrization is checked by plotting the parametrization functions of $\sigma_{L,T,LT,TT}$ versus the existing data and the VR model, as shown in Figs. 25, 26.

A.3 Parametrization of six Single-Spin Asymmetries

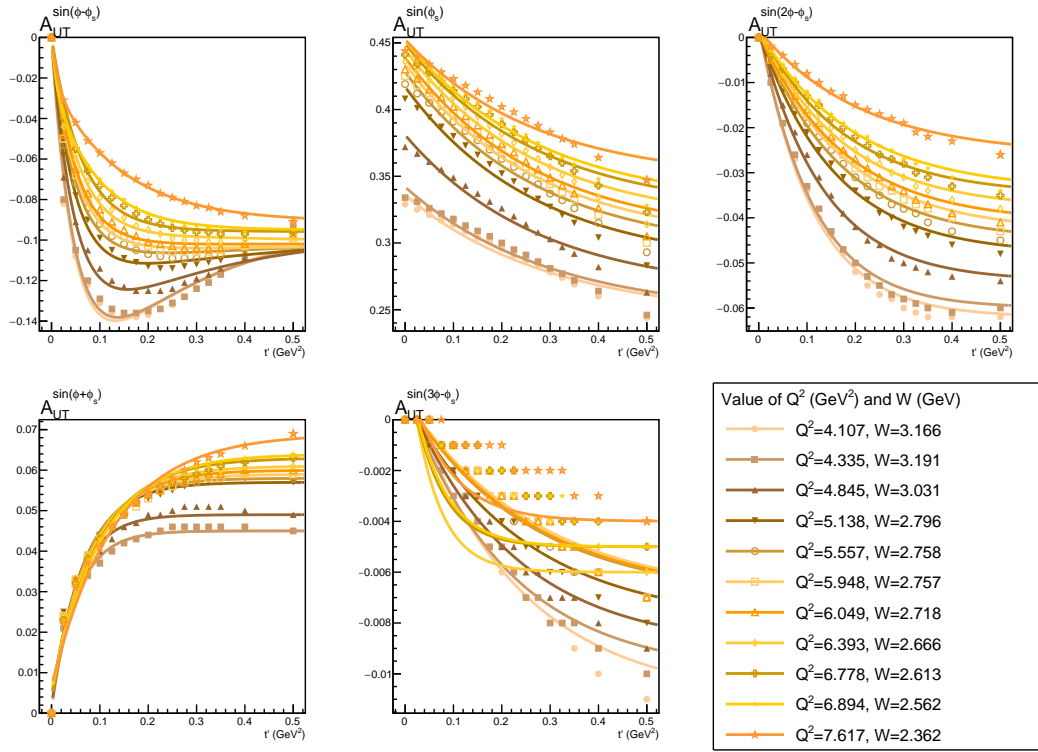


Figure 27: Parametrization of the five single spin asymmetries $A_{UT}^{\sin(\mu\phi+\lambda\phi_s)_k}$ vs. t' used in the event generator for this proposal. The points are the calculations by Goloskokov and Kroll [24] and the curves are our fit.

The single-spin asymmetries calculated for us by S.V Goloskokov and P. Kroll [24] have been used to approximate $d\sigma_{UT}$ in the DEMP event generator. Their $A_{UT}^{\sin(\mu\phi+\lambda\phi_s)_k}$ values are at discrete values of Q^2 from 4.107 to 7.167 GeV², W from 2.362 to 3.191 GeV, and t' from 0 GeV² to 0.5 GeV². There are six different azimuthal modulations defined as follows:

k	$\sin(\mu\phi + \lambda\phi_s)$
1	$\sin(\phi - \phi_s)$
2	$\sin(\phi + \phi_s)$
3	$\sin(\phi_s)$
4	$\sin(2\phi - \phi_s)$
5	$\sin(3\phi - \phi_s)$
6	$\sin(2\phi + \phi_s)$

These asymmetries are used to give

$$\Sigma_k = d\sigma_{UU}(\phi) A_{UT}^{\sin(\mu\phi + \lambda\phi_s)_k} \quad (36)$$

$$d\sigma_{UT} = -\frac{P_T}{\sqrt{1 - \sin^2\theta \sin^2\phi_s}} \sum_{k=1}^6 \sin(\mu\phi + \lambda\phi_s)_k \Sigma_k. \quad (37)$$

The $k = 6$ asymmetry ($(\mu, \lambda) = (2, 1)$) is not included in their calculation, and is taken to be zero, in accordance with the HERMES data (Fig. 11). The other five are calculated based on fits to their model values. The following fits were used:

$$A_{UT}^{\sin(\mu\phi + \lambda\phi_s)_k} = \begin{cases} ae^{bx} - (a+c)e^{dx} + c, & k = 1 \\ ae^{bx} + c, & k = 2, 3, 4, 5 \end{cases} \quad (38)$$

where a , b , c , and d are fit parameters. The forms of these functions were chosen only to closely match the shape of the simulated data and are not based on any physical principle. These fits are done for each given value of Q^2 independently, as shown in Fig. 27. During event generation, the asymmetry is calculated from the fit for the two nearest values of Q^2 . The asymmetry for the given event is then approximated by linear interpolation of the nearest values.

A.4 Target Neutron Fermi Momentum

A histogram of the spectral function of ${}^3\text{He}$ is shown in Fig. 28, generated according to Ref. [41]. Neutron momenta up to 300 MeV/c are generated according to this distribution, uniformly distributed in spherical coordinates. The quasi-free collision between the virtual photon and moving neutron is then transformed to the fixed neutron frame, after which the parameterizations of Secs. A.2.2, A.3 are applied. The outgoing particles are then transformed back to the lab frame for tracking.

A.5 Energy Loss and Multiple Scattering

There is energy loss for the incoming electron e , and the three outgoing particles: scattered electron e' , π^- and recoil proton p by bremsstrahlung and ionization. The same code as given in SAMC (Hall A Single Arm Monte Carlo) [42] is used. This code is based on Sec. 33 (Passage of articles through matter) of the Review of Particle Physics by the Particle Data Group [43].

The incoming electron and the three out going particles are deflected small angles by multiple scattering in the target, target window and in the air. This small deflection in the polar angle theta θ is calculated according to Subsection 33.3 (Multiple scattering through small angles) of the Review of Particle Physics by the Particle Data Group [43].

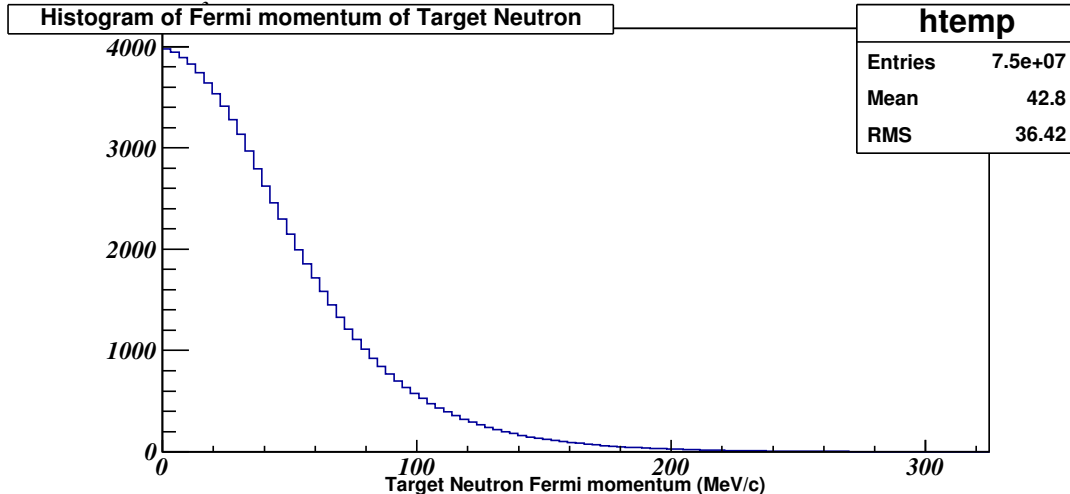


Figure 28: Fermi momentum spectral function of a target nucleon in ${}^3\text{He}$ generated according to the Argonne potential of Ref [41]. The horizontal axis is nucleon momentum in MeV/c.

The incoming electron loses energy by bremsstrahlung and ionization, and suffers multiple scattering, in the target and in the target window. Both of these processes and the choice of neutron Fermi momentum are applied before the cross section terms σ_{UU} and σ_{UT} are calculated from the ‘vertex’ kinematic quantities.

The scattered electron, pion and proton lose energy by bremsstrahlung and ionization, and suffer multiple scattering, in the target, target window and in the air. The energy and momentum of these particles are corrected according to these processes prior to particle tracking.

A.6 Final State Interactions

A separate version of the model was made in which the outgoing π^- suffers πN final state interactions (FSI) with one of the recoil p in the residual nucleus.

The scattering of π^- by protons involves both the $T = 1/2$ and $T = 3/2$ isospin states. We model the $\pi^- p$ scattering via the empirical phase shift analysis of Rowe, Solomon and Landau [44]. In this case, the amplitude for the scattering of a spin-zero particle by a particle of spin- $\frac{1}{2}$ is described for each isospin channel by a set of partial wave amplitudes $f_\ell^{(+)}$, $f_\ell^{(-)}$ for the $j = \ell \pm \frac{1}{2}$ states. In terms of phase shifts, $f_\ell^{(+)}$ is

$$f_\ell^{(+)} \equiv \frac{1}{2ik} (e^{2i\delta_\ell^+} - 1) \quad (39)$$

with a similar expression for $f_\ell^{(-)}$. The phase shift δ_ℓ^+ will be complex if there is any inelasticity, which will occur, for example, for the reactions:



The differential cross-section is written in terms of these phase shifts as

$$\frac{d\sigma}{d\Omega} = \left[\left| \frac{1}{k} \sum_{\ell} [(\ell+1)f_{\ell}^{(+)} + \ell f_{\ell}^{(-)}] P_{\ell}(\cos\theta) \right|^2 + \left| \frac{i}{k} \sum_{\ell} [f_{\ell}^{(+)} - f_{\ell}^{(-)}] \sin\theta \frac{dP_{\ell}(\cos\theta)}{d\cos\theta} \right|^2 \right]. \quad (41)$$

πN phase shifts have been determined experimentally from near threshold up to several GeV. The dominant phase shifts for the $L_{2T,2J}$ states: S_{11} , S_{31} , P_{11} , P_{13} , P_{31} , P_{33} are very accurately known for center of mass momenta up to 350 MeV/c. The phase shift parameterizations used in our model are dominated by the $\Delta(1232)$ and $N^*(1440)$ resonances. For further information, please see Ref. [45].

In our implementation of the FSI process, the Fermi momentum of one of the recoil protons was chosen according to Sec. A.4 and collided with the outgoing π^- in their mutual center of mass frame. Outgoing $\pi^- N$ were randomly generated, and the events weighted according to the differential cross sections of Eqn. 41. Events were generated for both the FSI and non-FSI versions of the model and the results compared, as described in the main text.

References

- [1] Approved SoLID SIDIS experiment E12-10-006, “Target Single Spin Asymmetry in Semi-Inclusive Deep-Inelastic ($e, e'\pi^\pm$) Reaction on a Transversely Polarized ^3He Target at 11 GeV”,
https://www.jlab.org/exp_prog/proposals/14/E12-10-006A.pdf
- [2] SoLID Collaboration, “Solenoidal Large Intensity Device Preliminary Conceptual Design Report”,
<http://hallaweb.jlab.org/12GeV/SoLID/files/solid-precdr.pdf>
- [3] M. Diehl, S. Sapeta, Eur. Phys. J. C **41** (2005) 515, arXiv:hep-ph/0503023.
- [4] A. Airapetian, Phys. Lett. **B 682** (2010) 345-350, arXiv:0907.2596 [hep-ex].
- [5] PR12-12-005: D. Dutta, D. Gaskell, W. Hersman, G.M. Huber, et al., “The Longitudinal Photon, Transverse Nucleon, Single-Spin Asymmetry in Exclusive Pion Production”.
- [6] M. Diehl, Contribution to the eRHIC White Paper, arXiv:hep-ph/0010200.
- [7] J.C. Collins, L. Frankfurt, M. Strikman, Phys. Rev. D **56** (1997) 2982.
- [8] K. Goeke, M.V. Polyakov, M. Vanderhaeghen, Prog. Part. Nucl. Phys. **47** (2001) 401-515.
- [9] A.V. Radyushkin, arXiv:hep-ph/0101225.
- [10] A.W. Thomas, W. Weise, “The Structure of the Nucleon”, J. Wiley-VCH, 2001.
- [11] R.E. Marshak, Riazuddin, C.P. Ryan, “Theory of Weak Interactions in Particle Physics”, J. Wiley, 1969.
- [12] M. Penttinen, M.V. Polyakov, K. Goeke, Phys. Rev. C **62** (2000) 014024 1-11.
- [13] A.V. Belitsky, D. Mueller, Phys. Lett. **B 513** (2001) 349-360.
- [14] S. V. Goloskokov and P. Kroll, Eur. Phys. J. C **65**, 137 (2010), arXiv:0906.0460 [hep-ph].
- [15] L.L. Frankfurt, P.V. Pobylitsa, M.V. Polyakov, M. Strikman, Phys. Rev. D **60** (1999) 014010 1-11.
- [16] M. Vanderhaeghen, P.A.M. Guichon, M. Guidal, Phys. Rev. D **60** (1999) 094017 1-28.
- [17] L.L. Frankfurt, M.V. Polyakov, M. Strikman, M. Vanderhaeghen, Phys. Rev. Lett. **84** (2000) 2589-2592.
- [18] A.V. Belitsky, CIPANP 2003 proceedings. arXiv: hep-ph/0307256.
- [19] C.E. Carlson, J. Milana, Phys. Rev. Lett. **65** (1990) 1717.
- [20] L. Mankiewicz, G. Piller, A. Radyushkin, Eur. Phys. J. C **10** (1999) 307-312.
- [21] E12-06-101, “Measurement of the Charged Pion Form Factor to High Q^2 ”, G.M. Huber, D. Gaskell, spokespersons.
- [22] Ivana Hristova, “Transverse-Target Single-Spin Azimuthal Asymmetry in Hard Exclusive Electroproduction of Single Pions at HERMES”, Ph.D. thesis, Humboldt University of Berlin, December 13, 2007.
<http://bib-pubdb1.desy.de/record/288884/files/desy-thesis-07-041.pdf?version=1>

- [23] pCDR for the Science and Experimental Equipment for the 12 GeV Upgrade of CEBAF, June, 2004.
V. Burkert, et al., PAC18 Review of the Science Driving the 12 GeV Upgrade, July, 2000.
- [24] S. V. Goloskokov and P. Kroll, private communications 2009-2017.
- [25] H.P. Blok, et al., Phys. Rev. C **78** (2008) 045202.
- [26] S. V. Goloskokov and P. Kroll, Eur. Phys. J. A **47**, (2011) 112, arXiv:1106.4897 [hep-ph].
- [27] Approved SoLID SIDIS experiment E12-11-007, “Asymmetries in Semi-Inclusive Deep-Inelastic ($e, e'\pi^\pm$) Reactions on a Longitudinally Polarized ^3He Target at 8.8 and 11 GeV”,
https://www.jlab.org/exp_prog/PACpage/PAC37/proposals/Proposals/New%20Proposals/PR-11-007.pdf
- [28] Approved SoLID SIDIS experiment E12-11-108, “Target Single Spin Asymmetry in Semi-Inclusive Deep-Inelastic ($e, e'\pi^\pm$) Reactions on a Transversely Polarized Proton Target”,
https://www.jlab.org/exp_prog/proposals/11/PR12-11-108.pdf
- [29] Approved SoLID J/ψ experiment E12-12-006A, “Near Threshold Electroproduction of J/ψ at 11 GeV”,
https://www.jlab.org/exp_prog/proposals/12/PR12-12-006.pdf
- [30] Approved SoLID SIDIS experiment E12-10-006A, “Dihadron Electroproduction in DIS with Transversely Polarized ^3He Target at 11 and 8.8 GeV”,
https://www.jlab.org/exp_prog/proposals/14/E12-10-006A.pdf
- [31] Approved SoLID SIDIS experiment E12-11-108A, “Target Single Spin Asymmetry Measurements in the Inclusive Deep-Inelastic $\vec{N}(e, e')$ Reaction on Transversely Polarized Proton and Neutron (^3He) Targets using the SoLID Spectrometer”
https://www.jlab.org/exp_prog/proposals/14/E12-11-108A_E12-10-006A.pdf
- [32] Approved SoLID PVDIS experiment E12-10-007, “Precision Measurement of Parity-violation in Deep Inelastic Scattering Over a Broad Kinematic Range”,
https://www.jlab.org/exp_prog/PACpage/PAC37/proposals/Proposals/Previously%20Approved/E12-10-007.pdf
- [33] J. L. Friar, et al., Phys. Rev. C **42** (1990) 2310;
C. Ciofi degli Atti, S. Scopetta, Phys. Lett. **B 404** (1997) 223;
R.W. Schulze, P.U. Sauer, Phys. Rev. C **56** (1997) 2293;
F. Bissey, A.W. Thomas, I.R. Afnan, Phys. Rev. C **64** (2001) 024004.
- [34] G. M. Huber, et al., Phys. Rev. C **91** (2015) 015202.
- [35] T. Horn, et al., Phys. Rev. Lett **97** (2006) 192001.
- [36] T. Horn, et al., Phys. Rev. C **78** (2008) 058201.
- [37] K. Park, et al., Eur. Phys. J. A **49** (2013) 16.
<http://clas.sinp.msu.ru/cgi-bin/jlab/db.cgi?eid=36;search=on>

- [38] A. Airapetian, et al., Phys. Lett. B. **659** (2008) 486.
- [39] A. Del Dotto, L.P. Kaptari, E. Pace, G. Salme, S. Scopetta, arXiv:1704.06182 [nucl-th].
- [40] T. Vrancx, J. Ryckebusch., Phys. Rev. C **89** (2014) 025203.
- [41] R. Schivavilla, V. R. Pandharipande., Nucl. Phys. **A 449** (1986) 219.
- [42] Hall-A Single-Arm Monte Carlo Simulation Tool,
<https://userweb.jlab.org/~yez/Work/SAMC/>
- [43] Particle Data Group, Chinese Phys. C **40** (2016) 100001.
- [44] G. Rowe, M. Solomon, R.H. Landau, Phys. Rev. C **18** (1978) 584.
- [45] T. Ericson, W. Weise, “Pions and Nuclei”, Oxford University Press, 1988.